Strength distribution of Ti/SiC metal-matrix composites under monotonic loading

Sivasambu Mahesh[a,*], Ashish Mishra[a]

[a] *Department of Aerospace Engineering, Indian Institute of Technology Madras, Chennai 600036. India.*

Abstract

The strength of metal matrix composites shows wide scatter on account of variability in the strengths of individual fibres. The relationship between the strength distribution of the fibres, and that of the composite is also affected by the non-linear matrix and fibre/matrix interfacial responses. The present study aims to describe the strength distribution of 2D and 3D commercial Ti/SiC composites. This is accomplished by performing Monte Carlo failure simulations of these composites, comprised of up to 128 fibres. A detailed deformation theory based model, developed and validated against experimental data in previous work, is used to calculate load redistribution in the course of each simulation. The empirical composite strength distribution obtained from the simulations follows weakest-link scaling. A stochastic model for the clustered propagation of fibre breaks, akin to a model proposed for polymer matrix composites in the literature, captures the empirical weakest-link strength distribution. A scaling relationship is derived between the composite strength and composite size for a number of reliability levels.

Keywords: Metal-matrix composite, Fracture, Statistical properties/methods, Monte Carlo Simulation

*Corresponding author

Email address: `smahesh@iitm.ac.in` (Sivasambu Mahesh)

1. Introduction

Substantial weight savings can be realised by replacing conventional metallic components in the hot stages of aerospace gas turbines with components made of metal matrix composites (Martin and Carrére, 2012). Yet, their adoption in practice has been limited, partly on account of their poor reliability (Singerman and Jackson, 1996). In order to overcome this limitation, developing a good understanding of the probabilisitic strength distribution of these materials, especially in the lower tail of the distribution, is necessary. Accessing the high reliability regime (probability of failure $\leq 10^{-6}$) through specimen testing requires a prohibitively large number of tests. However, a modelling methodology can yield the strength distribution in the high reliability regime. This methodology is based on obtaining mechanical and statistical insights into the dominant failure mechanisms, and deducing the probabilistic strength distribution from this information (Mahesh et al., 2002).

A well-developed reliability theory, based on an understanding of the dominant failure mechanism, exists for polymer matrix composites. The classical theory, which assumed linear material response has been summarised by Curtin (1998a) and by Phoenix and Beyerlein (2000). More recent work has focussed on accounting for the non-linear effects of matrix yielding and interfacial debonding/sliding. Okabe et al. (2001) developed a shear-lag model for polymer matrix composites, including these effects. Using Monte Carlo simulations, they predicted the size-scaling of the composite tensile strength. Their model, however, neglects the tensile stiffness of the matrix. The stress concentrations in the neighbours of a broken fibre are appreciably altered when the tensile stiffness of the matrix becomes comparable to that of the fibre. This was shown for the case of a composite with linear elastic phases, and a perfectly bonded fibre-matrix interface by Beyerlein and Landis (1999). In a metal matrix composite, the matrix and fibre stiffnesses are comparable. Therefore, the shear-lag model of Okabe et al. (2001) cannot directly be used.

Pimenta and Pinho (2013) proposed a hierarchical arrangement of failure events starting at the level of individual fibre breaks up to coupon-sized specimen failure. They derived analytical strength distributions based on this assumption. Behzadi et al. (2009) demonstrated the effect of matrix shear yielding on diminishing stress concentrations due to clusters of breaks through finite element analysis, and on the strength distribution through Monte Carlo simulations. Both Pimenta and Pinho (2013) and Behzadi et al. (2009) emphasise that the length scale of interest along the fibre direction increases with increasing size of transverse damage. A similar observation also emerges from the present study.

The reliability theories of metal matrix composites with weak interfaces also share many similarities with the well-developed theories for ceramic matrix composites. In a ceramic matrix composite, the load dropped by a broken fibre is equally distributed over the extent of the matrix crack, following global load sharing (Curtin, 1991; Phoenix and Raj, 1992). This renders the bundle strength Gaussian distributed. Curtin (1993) proposed that onset of global matrix plasticity in a metal matrix composite and extensive matrix cracking in ceramic matrix composites were analogous. On its basis, he deduced the tensile strength of metal matrix composites.

A detailed multiscale model of failure of a Ti/SiC composite was developed by Xia et al. (2001). Using finite element analysis, they obtained the stress field due to a single fibre break. Their finite element model realistically accounted for matrix plasticity and interfacial frictional sliding. However, due to computational limitations, they could only represent a few fibres in their finite element model. Xia et al. (2001) derived a Green's function from their single break finite element solution, and linearly superposed the Green's functions to obtain the stress-fields due to multiple breaks. They used this approach to update the stresses in their Monte Carlo fracture simulations. By this devise, they made the failure simulations computationally tractable. However, because the matrix and interface responses are strongly non-linear, the superposition principle does not apply. Linear superposition introduces significant non-conservative errors in the predicted stress fields due to multiple breaks. These errors then propagate into the composite strengths obtained from the failure simulations.

It is presently aimed to develop an understanding of the distribution of metal matrix composite strength for the case of a strong fibre/matrix interface. To this end, Monte Carlo failure simulations on more than 1000 computer composite 'specimen' have been performed on model composites. A typical specimen in these Monte Carlo simulations passes through a number of damaged states. Load redistribution is computed at each damaged state using a shear-lag model that accounts for fibre breakage, matrix cracking and plasticity, and interfacial debonding and sliding Mishra and Mahesh (2017). The most significant deviation from the earlier work of Xia et al. (2001) is that linear superposition is not presently employed to determine the stress fields in a damaged composite.

The Monte Carlo simulations yield empirical composite strength distributions, which obey weakest-link scaling, and show that the statistically dominant failure event is the growth of a cluster of breaks. This agrees well with the localised failure observed in these materials experimentally (Gundel and Wawner, 1997; González and Llorca, 2001; Ramamurty, 2005; Li et al., 2008). For example, González and Llorca (2001) found the failure of two neighbouring fibres to be the critical precursor of fracture. Furthermore, when the stress concentrations ahead of clusters of breaks are duly accounted for, the classical Harlow-Phoenix-Smith (Harlow and Phoenix, 1978a,b; Smith, 1980) stochastic model, developed for polymer matrix composites, is found to capture the empirical distributions.

2. The model composite specimen

2.1. Geometry and mechanical properties of the constituent phases

Fig. 1 shows an undamaged composite computer 'specimen' comprised of n_f fibres aligned with the z-axis. As detailed by Mishra and Mahesh (2017), the model specimen is comprised of parallel fibres, and intervening matrix. Two types of fibre arrangements in the cross-sectional plane, as shown in Fig. 2, are considered. These are henceforth referred to as two-dimensional (2D) and

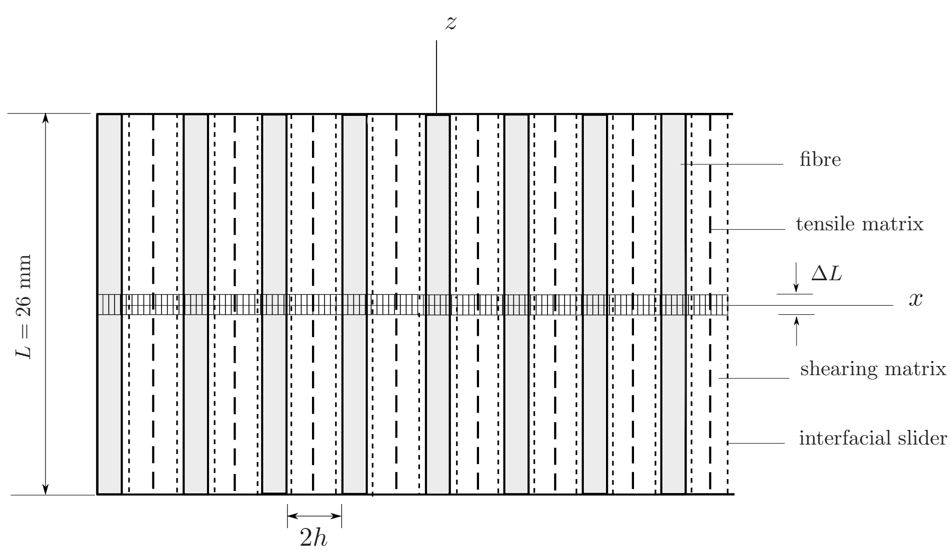

Figure 1: Model of an undamaged metal matrix composite ‘specimen’. Fibres are shown shaded dark. The matrix domain is divided into two parts: The ‘shear matrix’ is assumed to deform exclusively by shear, and the ‘tensile matrix’ in tension (dashed lines). Sliding displacements at the fibre matrix interface are permitted (dotted lines). A transverse ‘bundle’ of length ΔL, corresponding to the characteristic length of load transfer along the fibre direction is shown hatched. The x and z directions are shown scaled differently for clarity.

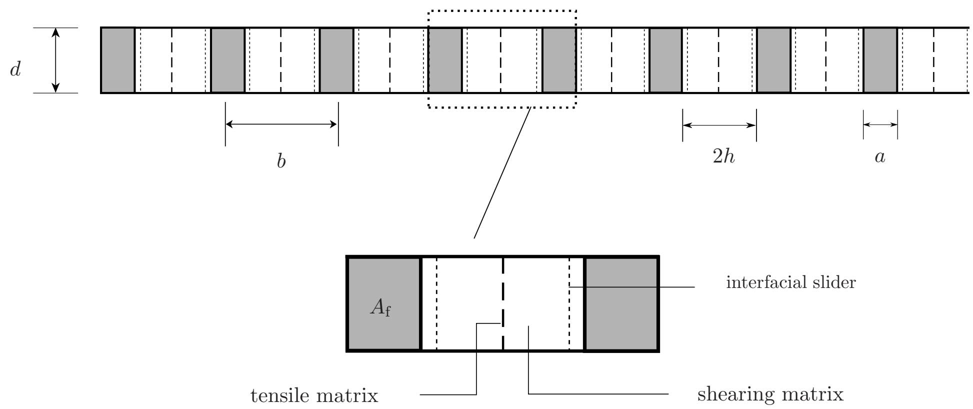

(a) 2D

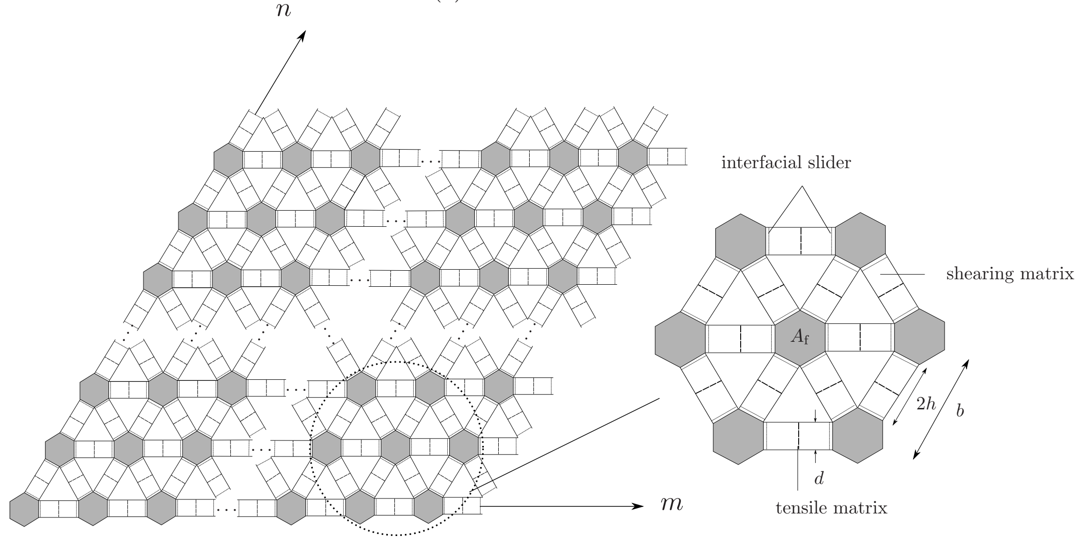

(b) 3D

Figure 2: Cross-section of the (a) 2D and (b) 3D model composites. The insets show the arrangement of the sliding elements, shear matrix elements, and tensile matrix elements between a pair of adjacent fibres. A_f denotes the fibre cross-sectional area.

three-dimensional (3D) composites, respectively. In the 2D composite tape, whose cross-section is shown in Fig. 2a, the fibres are positioned at regular intervals centred within a line segment. Each fibre has two neighbours. Fibres are identified by their position as f_i, $i \in \{0, 1, \ldots, n_\mathrm{f} - 1\}$. Adjacent fibres are connected together by a matrix strip. In the 3D composite, shown in Fig. 2b, the fibres are positioned at the points of a hexagonal lattice, contained within a rhombus-shaped domain. Adjacent edges of the rhombus coincide with the m- and n-axes, as shown. In this configuration, which is much more common in applications (Winstone et al., 2001; Martin and Carrére, 2012), each fibre is surrounded by six neighbours. Again, fibres are identified by their index, f_i, $i \in \{0, 1, \ldots, n_\mathrm{f} - 1\}$. It is assumed that the index i depends on the fibre coordinates (m, n) in the non-orthogonal mn coordinate system shown in Fig. 2b as

$$i = m\sqrt{n_\mathrm{f}} + n, \quad m, n \in \{0, 1, \ldots, \sqrt{n_\mathrm{f}} - 1\}. \tag{1}$$

As in the two-dimensional composite of Fig. 2a, matrix intervenes between every pair of adjacent fibres. It is clear from Fig. 2 that the number of intervening matrix elements,

$$n_\mathrm{tm} = \begin{cases} n_\mathrm{f}, & \text{in a 2D model composite, and} \\ 3n_\mathrm{f}, & \text{in a 3D model composite.} \end{cases} \tag{2}$$

In order to eliminate edge effects, the arrangement of fibres is assumed to be periodic in the transverse direction. In the 2D model composite of Fig. 2a, this amounts to assuming that the fibres at the left and right edges of the patch are neighbours. In the 3D composite of Fig. 2b, each fibre at the right edge of the rhombus patch ($m = \sqrt{n_\mathrm{f}} - 1$) is assumed to be a neighbour of the corresponding fibre located in the left edge ($m = 0$). Similarly, the fibres at the top ($n = \sqrt{n_\mathrm{f}} - 1$) and bottom ($n = 0$) edges of the rhombus patch are assumed to be neighbours.

As in Mishra and Mahesh (2017), the matrix intervening between adjacent fibres is treated as two separate entities termed tensile matrix and shear matrix. These entitites undergo axial and shear deformation, respectively. Although this decomposition considerably simplifies the model, it introduces the limitation that matrix yielding is not predicted based on a combined state of stress. The tensile matrix and shear matrix yield when their respective stresses attain the respective yield points. Interfacial sliding between a fibre and its abutting matrix is allowed. This is accounted for by introducing zero thickness sliding elements between the fibre and its abutting matrix element, as detailed in Mishra and Mahesh (2017).

Because the present model only represents the mechanically effective parts of the matrix, the model fibre volume fraction is typically greater than that of the actual specimen. The 2D model composite, shown in Fig. 2a, does not include the volumes devoid of fibres e.g., in the cladding Hanan et al. (2003) or Majumdar et al. (1998). Additionally, in 3D specimens, lightly stressed mechanically ineffective regions of the matrix may be present even in the fibre rich regions. These regions are represented by the empty equilateral triangles in Fig. 2b.

Model elements are assumed to displace only in the z-direction. The displacement fields in fibre f_i, tensile matrix tm_j and slider s_k at position z are denoted $w_{\mathrm{f}_i}(z)$, $w_{\mathrm{tm}_j}(z)$, and $w_{\mathrm{s}_k}(z)$, respectively. The stress and deformation states in the fibre, tensile matrix, shear matrix, and slider elements are assumed to be uniform in the transverse xy plane. Thus, the present model cannot capture transverse stress and deformation gradients in the fibre and matrix (Landis and McMeeking, 1999; Xia et al., 2001).

The following model details, which apply to both the 2D and 3D models, are recollected from Mishra and Mahesh (2017), as they are used in the sequel. Fibres are assumed to be brittle, and are taken to deform elastically obeying Hooke's law. Denoting the stress and strain at coordinate z in fibre f_i, $i \in \{0, 1, 2, \ldots, n_\mathrm{f} - 1\}$ by $\sigma_{\mathrm{f}_i}(z)$ and $\epsilon_{\mathrm{f}_i}(z)$, respectively, and the fibre modulus by E_f,

$$\sigma_{\mathrm{f}_i}(z) = E_\mathrm{f}\ \epsilon_{\mathrm{f}_i}(z). \tag{3}$$

Let $\sigma_{\mathrm{tm}_j}(z)$ and $\epsilon_{\mathrm{tm}_j}(z)$ denote the stress and strain at coordinate z in the

j-th tensile matrix bay, where $j \in \{0, 1, 2, \ldots, n_{\mathrm{tm}} - 1\}$. A deformation theory description is adopted for the stress-strain response of the tensile matrix:

$$\sigma_{\mathrm{tm}_j}(z) = \sigma_{\mathrm{Y}} \tanh\left(\frac{E_1 - E_2}{\sigma_{\mathrm{Y}}} \varepsilon_{\mathrm{tm}_j}(z)\right) + E_2 \varepsilon_{\mathrm{tm}_j}(z). \tag{4}$$

Here, E_1, E_2, and σ_{Y} denote the tensile Young's modulus, the hardening modulus of plastic deformation and yield strength of the matrix material, respectively. In order to determine if a tensile matrix material point is undergoing plastic loading or unloading, it is important to keep track of the maximum strain over the entire deformation history. This is denoted $\varepsilon^{\mathrm{peak}}_{\mathrm{tm}_j}(z)$. Loading corresponds to $\varepsilon_{\mathrm{tm}_j}(z) \geq \varepsilon^{\mathrm{peak}}_{\mathrm{tm}_j}(z)$. Eq. (4) is valid only in loading. If, however, the tensile matrix material point is unloading, i.e., $\varepsilon_{\mathrm{tm}_j}(z) < \varepsilon^{\mathrm{peak}}_{\mathrm{tm}_j}(z)$, a linear unloading constitutive law of the form

$$\sigma_{\mathrm{tm}_j}(z) = E_1(\varepsilon_{\mathrm{tm}_j}(z) - \varepsilon^{\mathrm{pl}}_{\mathrm{tm}_j}(z)), \tag{5}$$

is assumed for the material response. In Eq. (5), the plastic set, $\varepsilon^{\mathrm{pl}}_{\mathrm{tm}_j}(z)$ is defined as

$$\varepsilon^{\mathrm{pl}}_{\mathrm{tm}_j}(z) = \varepsilon^{\mathrm{peak}}_{\mathrm{tm}_j}(z) - \frac{\sigma^{\mathrm{peak}}_{\mathrm{tm}_j}(z)}{E_1}, \tag{6}$$

where, in turn,

$$\sigma^{\mathrm{peak}}_{\mathrm{tm}_j}(z) = \sigma_{\mathrm{Y}} \tanh\left(\frac{E_1 - E_2}{\sigma_{\mathrm{Y}}} \varepsilon^{\mathrm{peak}}_{\mathrm{tm}_j}(z)\right) + E_2\, \varepsilon^{\mathrm{peak}}_{\mathrm{tm}_j}(z). \tag{7}$$

In the present model, loads are conducted transverse to the fibre direction, by the shear matrix. Consider a shear matrix bay, sm_k. Let this shear matrix bay be abutted by fibre f_k, tensile matrix tm_k, and slider s_k (Fig. 1). Then, the shear strain γ_{sm_k} depends on the displacement of the abutting tensile matrix element w_{tm_k}, fibre w_{f_k} and slider element, w_{s_k} through

$$\gamma_{\mathrm{sm}_k} = \frac{w_{\mathrm{tm}_k} - w_{\mathrm{f}_k} - w_{\mathrm{s}_k}}{h}, \tag{8}$$

where $2h$ is the width of the matrix bay, as shown in Fig. 1. Arbitrary loading and unloading of the shear matrix is accounted for in analogy with the tensile matrix. In this case, shear stresses, strains, and moduli replace tensile stresses, strains and moduli of Eqs. (5)–(7), respectively. For example, the shear stress-strain relation under monotonic loading reads as

$$\tau_{\mathrm{sm}_k}(z) = \tau_{\mathrm{Y}} \tanh\left(\frac{G_1 - G_2}{\tau_{\mathrm{Y}}}\gamma_{\mathrm{sm}_k}(z)\right) + G_2\gamma_{\mathrm{sm}_k}(z). \tag{9}$$

Here, G_1, G_2, and τ_{Y} denote the shear modulus, the hardening modulus of plastic deformation under imposed shear and yield strength of the matrix material in simple shear, respectively.

In Ti/SiC fibre composites, there is little bonding between the fibre and matrix at the interface. But a large normal compressive stress is induced at the interface as the material is cooled from a high consolidation temperature to room temperature (Withers and Clarke, 1998). Frictional sliding is thus the primary mechanism of load transfer across the interface. The slider element s_k abutting shear matrix sm_k is assumed to obey the following laws of Coulomb friction:

$$w_{\mathrm{s}_k}(z) \begin{cases} \leq 0, & \text{if } \tau_{\mathrm{sm}_k}(z) < -\tau^*, \\ = 0, & \text{if } -\tau^* \leq \tau_{\mathrm{sm}_k}(z) \leq \tau^*, \\ \geq 0, & \text{if } \tau_{\mathrm{sm}_k}(z) > \tau^*. \end{cases} \tag{10}$$

Here, τ^* denotes the interfacial strength, which depends on the normal compressive interfacial stress introduced during material fabrication. The step function form of Eq. (10) makes it unsuitable for implementation in a gradient based solver. It is therefore regularised to obtain:

$$w_{\mathrm{s}_k}(z) = w_{s0}\left(\frac{\tau_{\mathrm{sm}_k}(z)}{\tau^*}\right)^{2n+1}. \tag{11}$$

where n is an integer rounding parameter, and w_{s0} is a scaling constant.

Fibre and tensile matrix element breaks in the present work are confined to the transverse plane $z = 0$, and the transverse planes $z = \pm L/2$ are subjected to uniform and equal displacements, $\pm w_0$ in opposite directions:

$$w_{\mathrm{f}_i}(z = \pm L/2) = w_{\mathrm{tm}_j}(z = \pm L/2) = \pm\, w_0, \tag{12}$$

for all $i \in \{0, 1, \ldots, n_{\mathrm{f}} - 1\}$ and $j \in \{0, 1, \ldots, n_{\mathrm{tm}} - 1\}$. On account of symmetry, it suffices to focus attention only on the region $0 \leq z \leq L/2$. Let $\varepsilon_{\mathrm{engg}} =$

$w_0/(L/2)$, denote the engineering strain imposed upon the composite. It is reasonable to assume that

$$\varepsilon_{\mathrm{f}_i}\left(z = L/2\right) \approx \varepsilon_{\mathrm{tm}_j}\left(z = L/2\right) \approx \varepsilon_{\mathrm{engg}}, \tag{13}$$

provided $L/2$ is large compared to the length scale of load recovery in broken tensile elements (Mishra and Mahesh, 2017). This assumption will be verified in Sec. 3.3.

Let P denote the applied axial composite load. Assuming all the tensile matrix elements at $z = L/2$ are in a state of loading, it follows from Eqs. (3), and (4) that the load per fibre, $p = P/n_{\mathrm{f}}$ is given as

$$\begin{aligned} p = \frac{A_{\mathrm{f}}}{n_{\mathrm{f}}} \sum_{i=0}^{n_{\mathrm{f}}-1} \left[E_{\mathrm{f}} \varepsilon_{\mathrm{f}_i} \left(z = \frac{L}{2} \right) \right] + \\ \frac{A_{\mathrm{tm}}}{n_{\mathrm{tm}}} \sum_{j=0}^{n_{\mathrm{tm}}-1} \left[\sigma_{\mathrm{Y}} \tanh\left(\frac{E_1 - E_2}{\sigma_{\mathrm{Y}}} \varepsilon_{\mathrm{tm}_j} \left(z = \frac{L}{2} \right) \right) + E_2 \varepsilon_{\mathrm{tm}_j} \left(z = \frac{L}{2} \right) \right]. \end{aligned} \tag{14}$$

Here, A_{f} and A_{tm} denote the cross-sectional areas of a fibre and a matrix bay, respectively. n_{f}, and n_{tm} denote the number of fibre and tensile matrix bays, respectively. Further, invoking the assumption of Eq. (13) leads to

$$p \approx A_{\mathrm{f}} E_{\mathrm{f}} \varepsilon_{\mathrm{engg}} + A_{\mathrm{tm}} \frac{n_{\mathrm{tm}}}{n_{\mathrm{f}}} \left[\sigma_{\mathrm{Y}} \tanh\left(\frac{E_1 - E_2}{\sigma_{\mathrm{Y}}} \varepsilon_{\mathrm{engg}} \right) + E_2 \varepsilon_{\mathrm{engg}} \right]. \tag{15}$$

It is straightforward to invert Eq. (15), in order to obtain the $\varepsilon_{\mathrm{engg}}$ corresponding to p using the numerical method of successive bisection.

The geometric and material parameters in the foregoing equations are assigned the same values as in Mishra and Mahesh (2017), which are listed in Table 1. The same parameters are used in both 2D and 3D model composites.

2.2. Composite strength distribution

Following Gücer and Gurland (1962), for the purpose of determining the strength distribution, $H_{n_{\mathrm{f}},L}(p)$, the composite is regarded as a 'chain of bundles'. The fibre-wise length of each bundle is denoted ΔL, as shown in Fig. 1. The bundles are assumed not to interact mechanically, i.e., fibre breaks in one bundle

Parameter	Value
Fiber area, A_f	0.0154 mm^2
Fibre spacing, b	240 μm
Ply thickness, d	124 μm
Fibre dimension, a	$A_\mathrm{f}/d = 124$ μm
Composite half guage-length, l	13 mm
Fiber elastic modulus, E_f	400 GPa
Matrix elastic tensile modulus, E_1	110 GPa
Matrix plastic tensile hardening, E_2	1.25 GPa
Matrix elastic shear modulus, G_1	42 GPa
Matrix plastic shear modulus, G_2	0.5 GPa
Matrix tensile yield stress σ_Y	820 MPa
Matrix shear yield stress τ_Y	550 MPa
Interfacial strength, τ^*	270 MPa
n	4

Table 1: Geometric and material parameters of the present model.

are assumed not to affect the stress-state in any other bundle. In experiments on Ti/SiC composites, (Gundel and Wawner, 1997; González and Llorca, 2001) it is found that fibre breaks are localised within a few fibre diameters of the fracture plane. Much of the damage prior to failure thus appears to be localised within a single bundle. The assumption of non-interaction between bundles is therefore well-satisfied by the present material.

Subject to the above assumptions, weakest-link considerations (Gücer and Gurland, 1962) imply that

$$H_{n_\mathrm{f},L}(p) = 1 - (1 - G_{n_\mathrm{f}}(p))^{(L/\Delta L)} . \tag{16}$$

It remains to determine $G_{n_\mathrm{f}}(p)$ through simulations and modelling.

2.3. Fibre strength distribution

In pristine SiC fibres with a smooth surface, failure nearly always initiates from the carbon core. The strength of such fibres is well described by the Weibull distribution. When embedded into a matrix, the in situ strengths of SiC fibres get modified (Li et al., 2008), as fibres develop surface damage during material fabrication. This is especially true for the present material, consolidated by hot pressing through the popular foil-fibre-foil technique.

Liu and Bowen (2003) have shown that the fibres in a similarly processed material have three distinct major failure modes. Accordingly, for SiC fibres, they proposed the trimodal Weibull strength distribution:

$$F(\sigma_{\mathrm{f}_i}; l) = 1 - \sum_{\iota=1}^{3} p_\iota \exp\left(-\frac{l}{l_0}\left(\frac{\sigma_{\mathrm{f}_i}}{\sigma_\iota^0}\right)^{m_\iota}\right) . \tag{17}$$

Here, l represents the gage length of the fibre, and $F(\sigma_{\mathrm{f}_i}; l)$ represents the probability of fibre failure under fibre stress σ_{f_i}. Liu and Bowen tested a number of fibre samples with gage length $l_0 = 40$ mm, and found that the parameters appropriate to virgin SCS-6 fibres are $p_1 = 7/63$, $p_2 = 15/63$, and $p_3 = 41/63$; $m_1 = 6.8$, $m_2 = 7.3$, and $m_3 = 14.6$; $\sigma_1^0 = 1781$ MPa, $\sigma_2^0 = 3240$ MPa, and $\sigma_3^0 = 4447$ MPa. In the foregoing, $\sum_{\iota=1}^{3} p_\iota = 1$. In terms of fibre strain, using

Eq. (3), Eq. (17) can be written as

$$F(\sigma_{\mathrm{f}_i}; l) = 1 - \sum_{\iota=1}^{3} p_\iota \exp\left(-\frac{l}{l_0}\left(\frac{E_{\mathrm{f}}\varepsilon_{\mathrm{f}_i}}{\sigma_\iota^0}\right)^{m_\iota}\right). \tag{18}$$

The mean fibre strength is

$$\langle\sigma_{\mathrm{f}_i}\rangle = \int_0^\infty \sigma_{\mathrm{f}_i}\frac{dF(\sigma_{\mathrm{f}_i}; l)}{d\sigma_{\mathrm{f}_i}} d\sigma_{\mathrm{f}_i} = \sum_{\iota=1}^{3} p_\iota \sigma_\iota^0 \left(\frac{l_0}{l}\right)^{1/m_\iota} \Gamma\left(1 + \frac{1}{m_\iota}\right). \tag{19}$$

Here, $\Gamma(t) = \int_{x=0}^{\infty} x^{t-1}e^{-x}dx$ denotes the gamma function (Abramowitz and Stegun, 2012).

2.4. Characteristic length

In the load sharing of ceramic matrix composites, an important dimension along the fibre direction is the characteristic length, δ_c (Henstenburg and Phoenix, 1989; Curtin, 1991). Let load recovery in a broken fibre occur through a uniform shear stress, τ, transmitted across a sliding interface. Then, the characteristic length of load recovery at a characteristic stress σ_c is given by $\delta_c = r\sigma_c/\tau$. In this expression, r is the fibre radius, and σ_c itself is the mean strength of length δ_c of fibre. Substituting this condition into Eq. (19) yields

$$\sigma_c = \sum_{\iota=1}^{3} p_\iota \sigma_\iota^0 \left(\frac{l_0}{\delta_c}\right)^{\frac{1}{m_\iota}} \Gamma\left(1 + \frac{1}{m_\iota}\right) = \sum_{\iota=1}^{3} p_\iota \sigma_\iota^0 \left(\frac{l_0}{r\sigma_c/\tau}\right)^{\frac{1}{m_\iota}} \Gamma\left(1 + \frac{1}{m_\iota}\right), \tag{20}$$

a non-linear algebraic equation for the unknown σ_c. In the strength theory of ceramic matrix composites (Curtin, 1991) fibre breaks more than δ_c apart in the z-direction are regarded as non-interacting.

Substituting the statistical parameters obtained by Liu and Bowen (2003) into Eq. (20) yields $\sigma_c \approx 5000$ MPa. Taking $\tau = 270$ MPa, and $r = 70$ μm for the SCS-6 fibres (Mishra and Mahesh, 2017), $\delta_c \approx 1.3$ mm is obtained. According to the theory of Curtin (1993) and Xia et al. (2001), it is reasonable to take the length of a bundle, $\Delta L = \delta_c$ in Fig. 1. Fibre breaks separated axially by more than δ_c are assumed to be non-interacting (Curtin, 1991; Phoenix and Raj, 1992). A similar assumption has been made by Xia et al. (2001) in Monte Carlo simulations of titanium matrix composites. Thus, the composite is regarded as a chain of L/δ_c bundles, each of length $\Delta L = \delta_c$.

2.5. Monte Carlo composite failure simulations

The purpose of the Monte Carlo simulations is to determine the strength distribution, $G_{n_\mathrm{f}}(p)$, of a single bundle, spanning $-(\Delta L/2) \leq z \leq (\Delta L/2)$. This bundle is shown hatched in Fig. 1. Each fibre in this bundle is assigned a random strength drawn from Liu-Bowen's extended Weibull distribution, Eq. (17), with $l = \Delta L$. A fibre breaks when its stress equals its strength. The failure strain of tensile matrix elements is assumed to be deterministic. Tensile matrix j fails when $\varepsilon_{\mathrm{tm}_j}(z = 0)$ reaches a preset strain limit, which is arbitrarily taken to be 1.5 times the yield strain. The predicted strength distributions are found to insensitive to this factor. Fibre and tensile matrix breaks are restricted to the plane $z = 0$. This assumption is conservative because the stress concentration ahead of staggered breaks is smaller than that ahead of breaks aligned in the transverse plane $z = 0$. Further, the stress distribution will be symmetric about the plane $z = 0$. Therefore, only half the specimen ($0 \leq z \leq L/2$) needs to be analysed. The number of fibres, n_f, in the simulation cell is, however, variable. Four sizes are presently considered in 2D composite simulations: $n_\mathrm{f} = 32$, 64, 96, and 128, and two sizes in 3D composite simulations: $n_\mathrm{f} = 36$, and 64.

To obtain stable crack propagation, computer simulated tensile tests are performed under displacement control imposed at $z = L/2$. Each simulation is sub-divided into a number of steps. At the beginning of each step, the residual strength of each fibre and tensile matrix element is determined. The residual strength is the additional stress that a fibre or tensile matrix element requires in order to fail, starting from the current state. The minimum increment in the far-field displacement needed to fail at least one more fibre or tensile matrix element of length ΔL at $z = 0$ is determined by solving a reduced linear model (Mishra and Mahesh, 2017). An elastoplastic analysis, detailed by Mishra and Mahesh (2017), is then performed over this displacement increment. The displacement and stress state in all the elements are updated. It is then checked if the strength of any fibre or tensile matrix element is exceeded. If so, those elements are also broken and the elastoplastic state is reanalysed. The residual strengths are then determined, and the far-field displacements are incremented, as before. The simulation terminates when the number of broken fibres exceeds $n_{\mathrm{f}}/3$.

Following the ‘chain of bundles’ assumption, a fibre break is introduced at $z = 0$ if the stress at $z = 0$ equals the randomly assigned strength of a ΔL segment of the fibre. This assumption amounts to assuming that the broken fibre regains no load over the entire ΔL length of the bundle, and that the stress concentration over intact fibres within a layer equals the maximum value realised at $z = 0$. Experimental observations suggest that this is a good approximation for the present Ti/SiC composite. González and Llorca (2001, Fig. 3) observed two or three fibre cracks in each fibre spaced 0.1–0.3 mm apart, near the specimen fracture plane. Similar observations have also been reported by Majumdar et al. (1998) and Gundel and Wawner (1997). These fibre breaks would unload most of the length ΔL in the broken fibre, in accord with the ‘chain of bundles’ idealisation.

Curtin (2000) compared the ‘chain of bundles’ model with a pull out model of load transfer, and found that the mean composite strength may be underestimated by as much as 25%. To arrive at this result, Curtin (2000) assumed a single centrally located break in each ΔL segment of the fibre, and that load is regained following a triangular profile within the ΔL bundle. Since the experimental observations noted above differ significantly from these assumptions, it is expected that the composite strength is not as underestimated by the present ‘chain of bundles’ model as predicted by Curtin (2000). In fact, it is found later in Sec. 3.8 that the mean strength is underestimated by as little as 3% in a 3D composite.

3. Results and discussion

Following the classical linear elastic shear-lag models, Mishra and Mahesh (2017) introduced the elastic recovery length along the fibre direction

$$K^{1/2} = \left(\frac{G_1}{\sqrt{h^2 A_{\mathrm{tm}} E_{\mathrm{f}} E_1}} \right)^{1/2}. \tag{21}$$

In the sequel, the applied load per fibre, and the imposed engineering strain are normalised as

$$\hat{p} = \frac{pW}{E_{\mathrm{f}} A_{\mathrm{f}}}, \tag{22}$$

and

$$\hat{\varepsilon}_{\mathrm{engg}} = \varepsilon_{\mathrm{engg}} W, \tag{23}$$

where, $W = \frac{G_1 - G_2}{\tau_Y} \frac{1}{h\sqrt{K}}$. Similarly, the fibre and tensile matrix strains are normalised as $\hat{\varepsilon}_{\mathrm{f}_i} = \varepsilon_{\mathrm{f}_i} W$, and $\hat{\varepsilon}_{\mathrm{tm}_j} = \varepsilon_{\mathrm{tm}_j} W$. The normalised quantities are of the order of unity.

3.1. Bundle length

A common assumption in the literature, e.g., (Beyerlein and Phoenix, 1996; Mahesh and Phoenix, 2004; Behzadi et al., 2009), maintains that the bundle length, ΔL, is given by the fibre-wise distance over which the stress in an intact fibre adjacent to a single break exceeds the far-field stress. Thus, if z_c is a critical distance such that $\varepsilon_{\mathrm{f}_1}(\pm z_c)/\langle \varepsilon_{\mathrm{f}_i}(z = L/2) \rangle = 1$, it is typically assumed that $\Delta L = 2z_c$.

Fig. 3a shows the strain profiles in all the fibres of the $n_{\mathrm{f}} = 128$ fibre composite with a single break placed at $z = 0$ in fibre f_0. Sufficient far-field displacement is imposed to induce gross yielding of the matrix. Fig. 3a shows that $z_c = 0.57$ mm. Interestingly, $z_c \approx \delta_c/2 = 0.65$ mm. That is, the assumption that $\Delta L = \delta_c$, derived from considerations originally applied to ceramic matrix composites, is nearly consistent with that obtained from the load decay ahead of a single break.

With increasing number of breaks in the cluster, the critical distance over which the neighbouring intact fibre is overloaded also increases. For clusters of

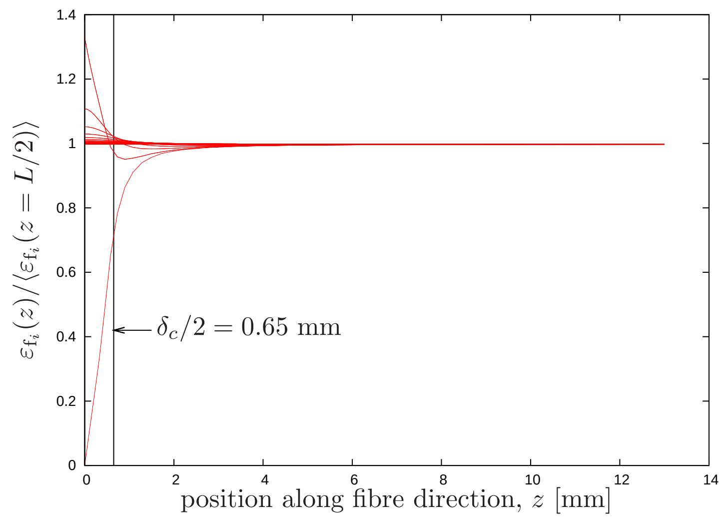

(a) $k = 1$

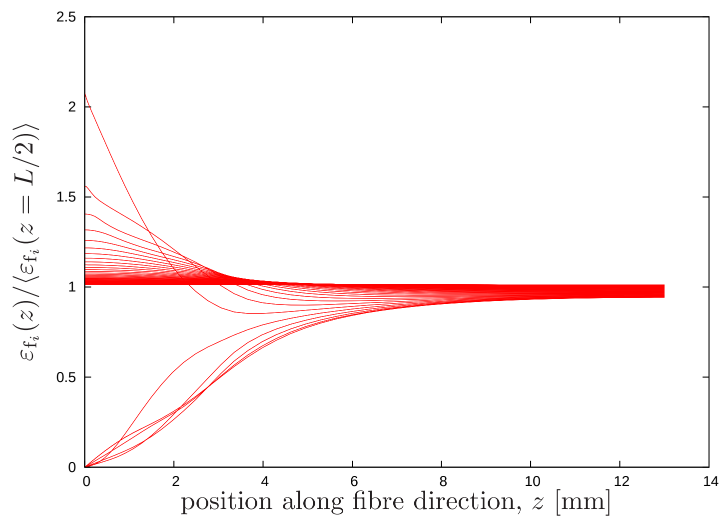

(b) $k = 10$

Figure 3: Fibre overstrain profiles in all the fibres ($i \in \{1, 2 \ldots, n_\mathrm{f}\}$) under imposed strain $\hat{\varepsilon}_{\mathrm{engg}} = 2.55$ in an $n_\mathrm{f} = 128$ fibre composite with (a) $k = 1$, and (b) $k = 10$ cluster of breaks. The imposed strain is sufficiently large to cause gross matrix yielding in the specimen.

two and three breaks, for instance, $z_c = 0.86$ mm and 1.07 mm, respectively. As seen in Fig. 3b, the critical distance of stress decay is in excess of 2 mm ahead of a cluster of $k = 10$ breaks. In fact, the load in the broken fibres does not fully recover, even at the end of the gage section located at $z = L/2 =$ 13 mm. Clearly, as the size of the cluster of breaks increases, the assumption of mechanical non-interaction between breaks separated by more than δ_c along the z-direction becomes increasingly invalid. However, it must be noted that the assumption of non-interaction is conservative, i.e., leads to a larger failure probability, $H_{n_{\mathrm{f}},L}(p)$. Accordingly, the chain-of-bundles assumption (Eq. (16)) is presently adopted.

3.2. Empirical strength distribution

Figs. 4a and 4b show the cumulative distribution functions of bundle strength, $G_{n_{\mathrm{f}}}(p)$ of 2D and 3D model composites, respectively. The 2D empirical distribution functions are obtained from $n_{\mathrm{sim}} = 250$ computer simulated Monte Carlo tensile tests of statistically identical composite specimen comprised of $n_{\mathrm{f}} = 32$, 64, and 96 fibres. $n_{\mathrm{sim}} = 303$ simulations were performed on composites comprised of $n_{\mathrm{f}} = 128$ fibres. 3D empirical distributions were obtained from $n_{\mathrm{sim}} = 250$ computer simulated Monte Carlo tensile tests of model composites with $n_{\mathrm{f}} = 36$, and 64.

In the coordinates of the normal probability paper used in Fig. 4, Gaussian distributions plot as straight lines. The horizontal intercept of the straight line corresponds to the mean of the distribution and the reciprocal of its slope corresponds to the standard deviation. The obtained empirical strength distributions shown in Fig. 4 are apparently Gaussian distributed. Both mean strength of the bundle per fibre, $\langle \hat{p} \rangle$ (x-intercept) and standard deviation (reciprocal slope) decrease with increasing n_{f}.

A classical result due to Daniels (1945) states that the strength of a loose (equal load sharing) bundle of threads is Gaussian distributed. The mean strength per fibre of Daniels' bundles are, however, independent of n_{f} to leading order. At higher order, they decrease as $n_{\mathrm{f}}^{-2/3}$ with a small pre-factor

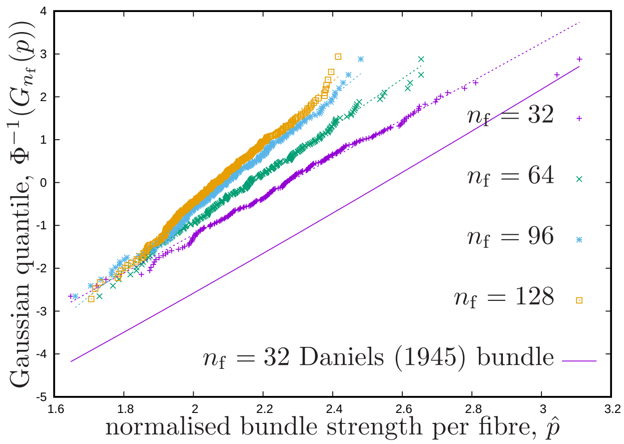

(a) 2D

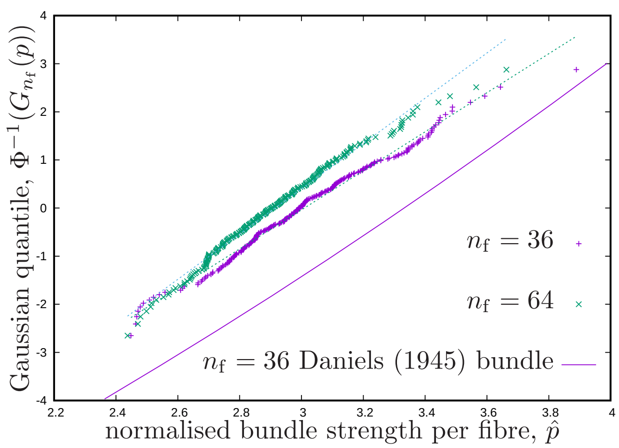

(b) 3D

Figure 4: Empirical cumulative distribution functions of bundle strength, $G_{n_f}(p)$, plotted on normal probability paper for (a) 2D, and (b) 3D model composites. These distributions are obtained from Monte Carlo simulations. $\Phi(\cdot)$ denotes the standard normal distribution function with zero mean and unit standard deviation. Dashed lines represent linear least squares fits of the empirical distributions. The solid line depicts the strength distribution of a loose bundles, as predicted by Daniels (1945) for $n_f = 32$ fibres in (a), and $n_f = 36$ fibres in (b).

(McCartney and Smith, 1983; Phoenix and Raj, 1992). The mean strength per fibre of the present model bundles decrease with increasing n_f much more rapidly. Therefore, the statistics of the present bundles differ qualitatively from those of Daniels' bundles. Nevertheless, the standard deviation of strength of the $n_\mathrm{f} = 32$, 2D bundle, $G_{n_\mathrm{f}=32}(p)$, agrees closely with that of a Daniels bundle comprised of the same number of fibres (Fig. 4a). The empirical distribution functions and the strength distributions of larger Daniels bundles deviate substantially. In 3D, the standard deviation of strength of an $n_\mathrm{f} = 36$ fibre composite is already greater than that of an $n_\mathrm{f} = 36$ Daniels bundle.

3.3. Failure mode

Fig. 5 shows the normalised load-displacement curves at $z = L/2$ corresponding to two $n_\mathrm{f} = 128$ 2D computer specimens. The two graphs correspond to the strongest and weakest specimens of $n_\mathrm{sim} = 303$ simulations. Fig. 5 also shows the accumulation of fibre breaks with applied far-field displacement. Initially, fibre breaks accumulate gradually with increasing imposed engineering strain. Over this regime, the load-displacement curves remain approximately linear, in accord e.g., with the experimental observation of Withers and Clarke (1998). However, at a critical applied engineering strain, which also corresponds to the maximum applied load, a large number of fibre breaks suddenly appear. In both the specimen of Fig. 5, this increases the material compliance sufficiently to decrease the applied load, as the computer simulations are performed under displacement control. Under load control, the burst of fibre breakages observed at the peak load would correspond to unstable crack propagation, and specimen fracture. The failure of the simulated composites thus has a brittle character.

The evolution of the normalised mean fibre and tensile matrix strains at $z = L/2$ with the normalised imposed engineering strain in the strongest and weakest specimen are shown in Fig. 6. It is seen that up to the peak $\hat{\varepsilon}_\mathrm{engg}$ the mean fibre and tensile matrix strains at $z = L/2$ equal the engineering strain. In other words, the increase in specimen compliance due to fibre and tensile matrix breaking prior to the peak load is negligible. However, once the

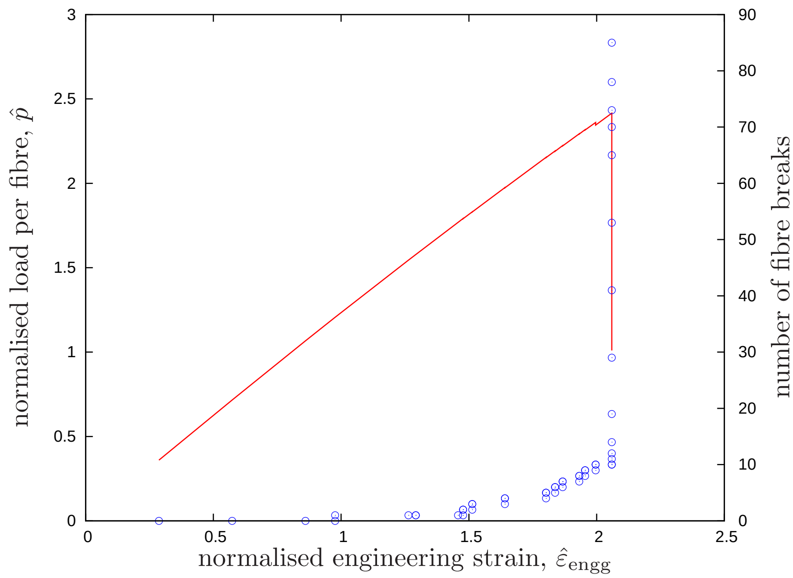

(a) Strongest of 303 specimen

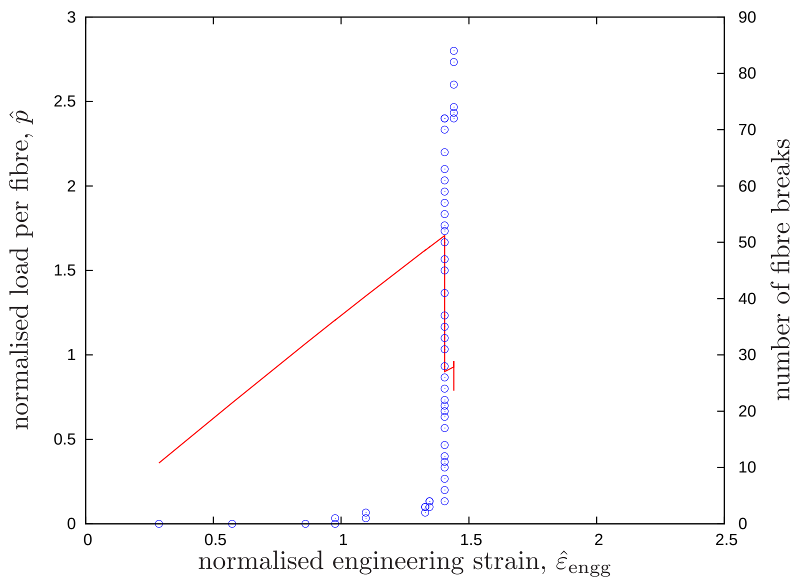

(b) Weakest of 303 specimen

Figure 5: Variation of the applied normalised load per fibre, $\hat{p}$ over the course of a Monte Carlo simulation of failure in the (a) strongest, and (b) weakest of 303 computer specimen. Each composite is comprised of n_{f} fibres. The circles indicate the number of fibre breaks.

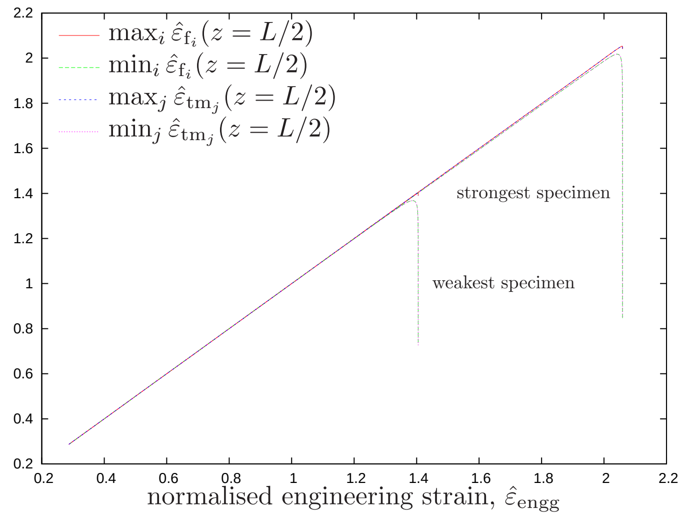

Figure 6: Evolution of the average normalised fibre and tensile matrix strain at $z = L/2$ with imposed engineering strain during the simulation of the strongest and weakest 128 fibre 2D specimen.

peak load is reached, catastrophic fibre breakage causes an abrupt increase of the specimen compliance. The mean fibre and tensile matrix strains at $z = L/2$ then drop abruptly at constant $\hat{\varepsilon}_{\mathrm{engg}}$. These observations validate the assumption of Eq. (13), up until the peak load is reached.

The step-by-step (Sec. 2.5) evolution of the spatial distribution of the fibre and tensile matrix breaks in the strongest and weakest $n_{\mathrm{f}} = 128$-fibre 2D composite specimen is depicted in Fig. 7. As noted previously, some steps involve only an evolution of the elastoplastic fields in the composite; no additional fibre or tensile matrix breakage occurs in them. The step at which the peak load is imposed is indicated by a vertical dotted line in Fig. 7. In both the strongest and weakest specimen, the fibre breaks formed before the peak applied load is reached, appear positionally uncorrelated. This is similar to the pattern of breaks in a Daniels (1945) bundle. Soon after a fibre breaks, the pair of tensile matrix elements flanking the fibre nearly always break. Thus, the matrix directly contributes little to the composite toughness. This observation, in conjunction with the observations of Pini et al. (2017) suggests that the present

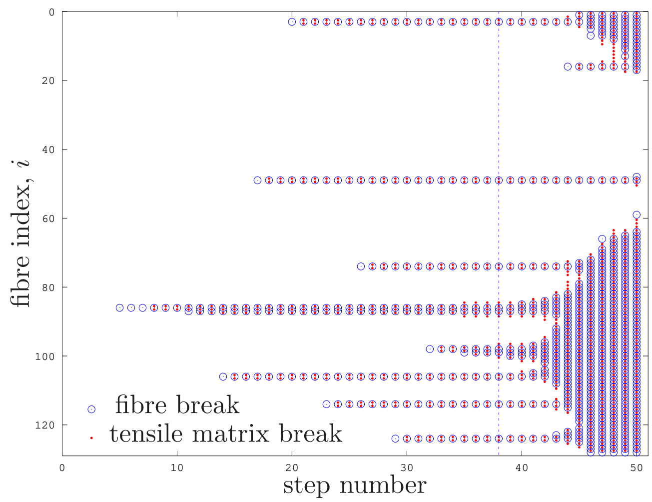

(a) Strongest of 303 specimen

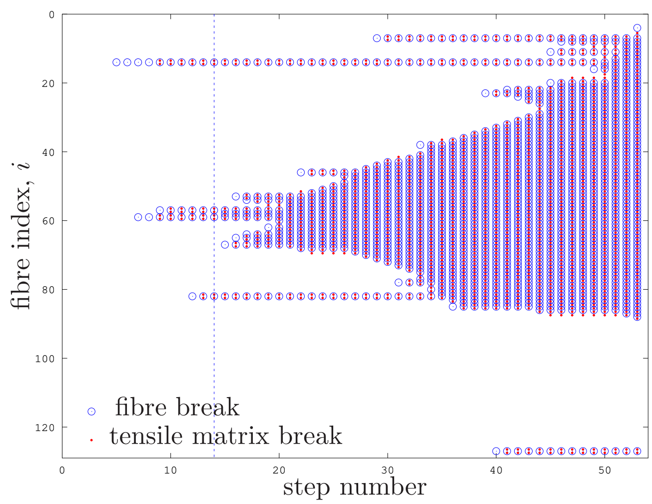

(b) Weakest of 303 specimen

Figure 7: Progression of breaks in the fibre (large circles) and tensile matrix (small dots) elements over the course of a Monte Carlo simulation of failure in the (a) strongest and (b) weakest $n_\mathrm{f} = 128$-fibre 2D specimens of 303 computer specimen. The vertical dotted line denotes the step beyond which further breaks occur with no increase in applied load. No fibre or tensile matrix element breakage occur in some steps; they involve only evolution of the elastoplastic state, and/or of the interfacial sliding displacement.

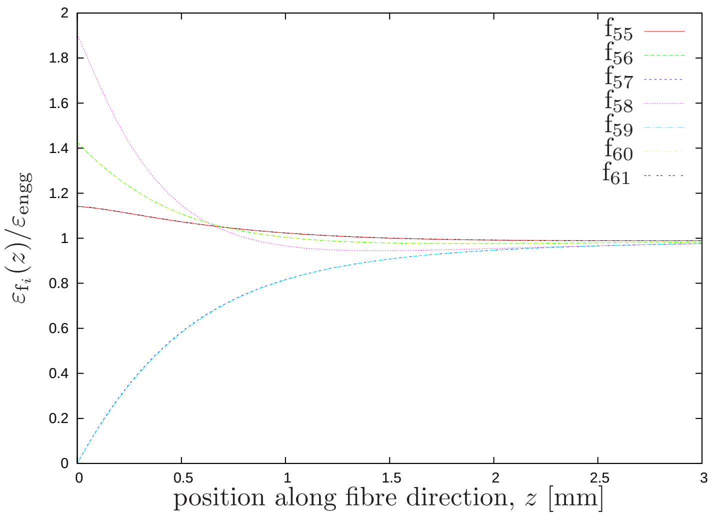

Figure 8: Normalised fibre strains near the critical cluster of breaks at peak load (step 14) in the weakest 128-fibre 2D specimen.

composite may be toughened by strengthening the matrix.

At some step during the simulation, uncorrelated fibre breakage ceases, and gives way to the propagation of a cluster of fibre breaks, starting from one of the initial 'seed' fibre breaks. This happens at the peak load. In both the strongest and weakest specimen, this propagation occurs, in part, by the coalescence of the main cluster of breaks with small clusters ahead of itself. The observed clustered sequence of fibre failures agrees with the observations of Gundel and Wawner (1997), and González and Llorca (2001).

3.4. Elastoplastic fields at peak load

The elastoplastic fields at the peak load (step 14) in the weakest 128-fibre 2D specimen are next considered. As seen in Fig. 7b, the cluster of breaks that extends catastrophically is comprised of two fibre breaks in fibres f_{57} and f_{59}, and tensile matrix breaks in tm_{57}, tm_{58}, tm_{59}, and tm_{60}. Fig. 8 shows the fibre strains near the broken fibres. The greatest strain concentration occurs in f_{58}. Under the influence of this intense stress concentration, fibre f_{58} breaks in the next step. The next largest strain concentrations are observed in fibres f_{56} and

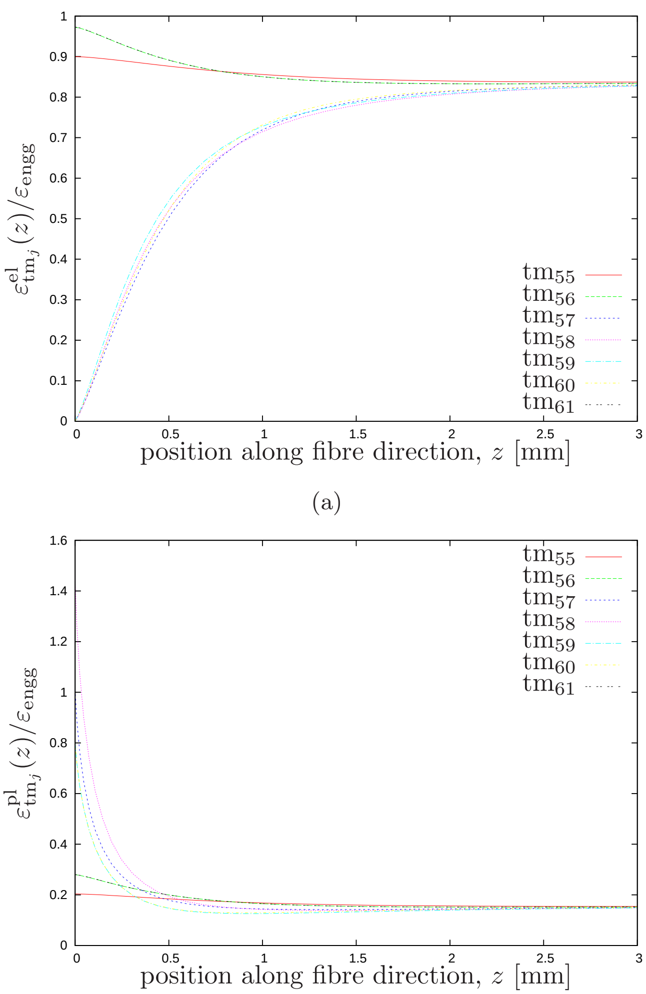

(a)

(b)

Figure 9: (a) Elastic and (b) plastic normalised strains in the tensile matrix, near the critical cluster of breaks at peak load (step 14) in the weakest 128-fibre 2D specimen.

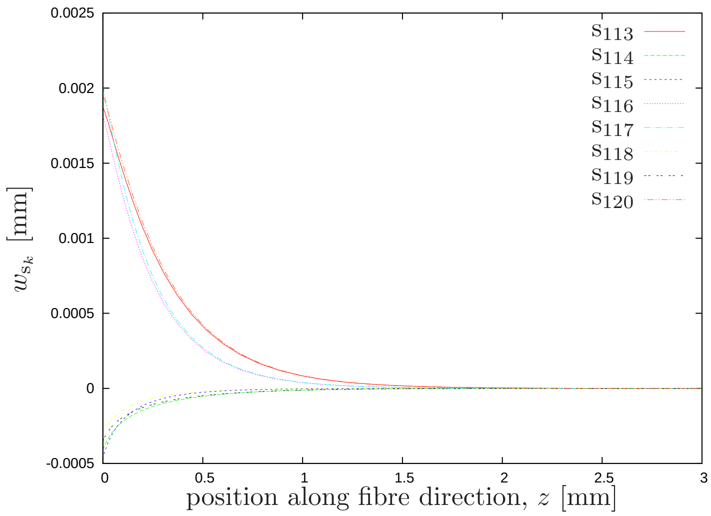

Figure 10: Sliding displacements, w_{s_k}, near the critical cluster of breaks at peak load (step 14) in the weakest 128-fibre 2D specimen.

f_{60}, which also fail shortly after step 14 (peak load).

Fig. 9 shows the elastic and plastic strains in the tensile matrix elements near the presently considered cluster of breaks. The elastic strain concentrations in the tensile matrix elements (Fig. 9a) are generally smaller than that in the corresponding fibres. In fact, the elastic strains are all smaller than even the imposed engineering strain. However, the plastic strain concentrations are much larger, as shown in Fig. 9b. The large plastic deformation shields the tensile matrix elements from high stresses.

Fig. 10 shows the slider element displacements in the vicinity of the breaks. Slider element s_{113} is abutted by the broken tm_{57}, and intact fibre f_{56}. This produces sliding of about 2 μm in s_{113}, at the plane $z = 0$ mm and thereby shields f_{56} from intense stress concentration. The other sliders that also develop high sliding displacements, s_{116}, s_{117}, and s_{120} are also abutted by one intact and one broken tensile member. On the other hand, slider elements s_{114}, s_{115}, and s_{119}, which experience relatively smaller sliding displacements are abutted by tensile elements that are both broken. It can be inferred that sliding is a mechanism to blunt intense localisation of stress concentrations between broken and intact tensile elements in the model.

The present discussion has been restricted to 2D composites. The observations, however, carry over qualitatively to 3D composites as well.

3.5. Stress redistribution due to a tight cluster of breaks

The notion of a tight cluster of breaks is due to Smith et al. (1983). In both 2D and 3D composites, a tight cluster of breaks is defined inductively, beginning with a single break, $k = 1$. A tight cluster of $k > 1$ breaks is constructed from a tight cluster of $k - 1$ breaks by breaking any one of the most overloaded intact fibres surrounding the $(k - 1)$-tight cluster. Any tensile matrix element neighbouring a broken fibre is also broken. In 2D composites, this definition simply results in a linear array of k adjacent broken fibres, e.g., f_i, $i = 1, 2, \ldots, k$, and in $k + 1$ adjacent broken tensile matrix elements in tm_j, $j = 1, 2, \ldots, k + 1$, at $z = 0$. The progression of tight cluster growth in the 3D composite up to $k = 7$ is shown in the inset of Fig. 11b.

The stress concentration ahead of a k-cluster of breaks in the plane $z = 0$ in 2D and 3D composites is defined as:

$$K_k = \max_{i=1}^{n_\mathrm{f}} \varepsilon_{\mathrm{f}_i}(z = 0) \Bigg/ \left(\sum_{i=1}^{n_\mathrm{f}} \varepsilon_{\mathrm{f}_i}(z = L/2)/n_\mathrm{f} \right) , \tag{24}$$

where f_i denotes the i-th fibre in the composite patch. The denominator in this expression denotes the average far-field fibre strain. Because of material non-linearities associated with the matrix and the interface, the stress concentration, K_k depends also on the imposed strain, $\hat{\varepsilon}_\mathrm{engg}$. Figs. 11a, and 11b show K_k for cluster sizes $k = 1, 2, \ldots, 10$ at various imposed engineering strains, which span the range of failure strains observed in the Monte Carlo simulations, respectively. It is clear that at a fixed imposed engineering strain, K_k increases monotonically with increasing k. Also, K_k decreases monotonically with the imposed engineering strains, for a given cluster size, k.

Over the range of cluster sizes and imposed strains investigated in Fig. 11, the computed stress concentrations, K_k can be bounded from above and below

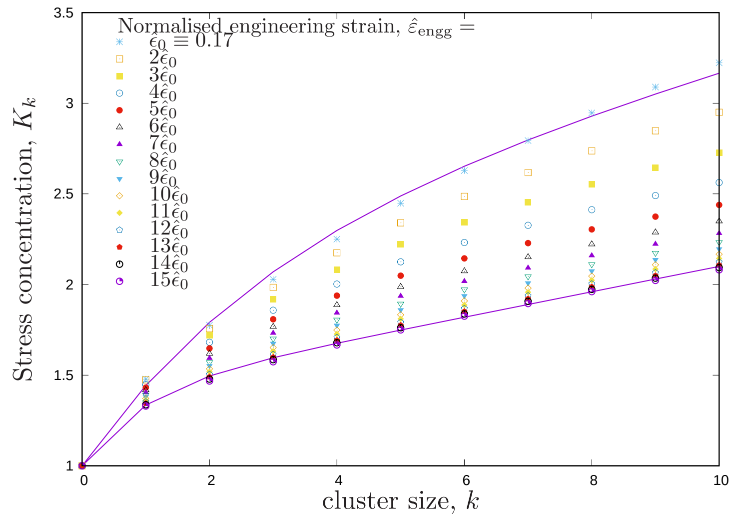

(a) 2D

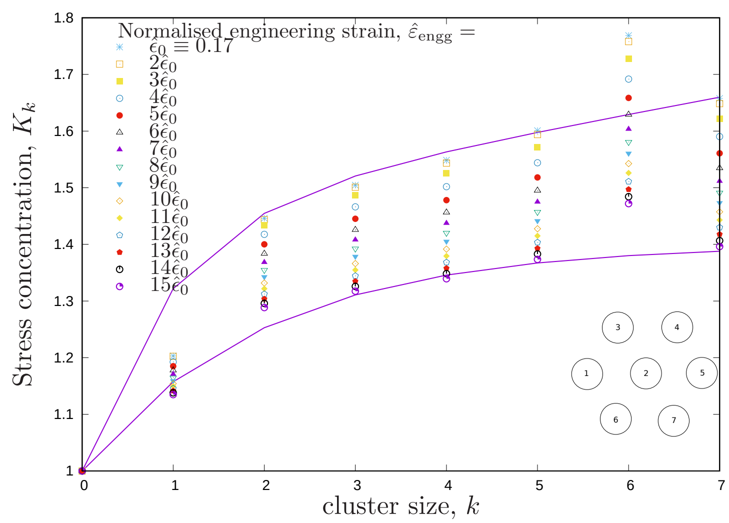

(b) 3D; inset shows tight cluster growth up to $k = 7$ breaks.

Figure 11: Stress concentration, defined in Eq. (24), in the first intact fibre ahead of a cluster of k fibre breaks in (a) 2D and (b) 3D model composites. Because of material non-linearities associated with the matrix and the interface, the stress concentration depends also on the imposed strain, $\hat{\varepsilon}_{\mathrm{engg}}$. Over the present range of cluster sizes and imposed strains, the stress concentration can be bounded by two analytical curves, shown by solid lines.

	2D		3D	
Parameter	Lower bound	Upper bound	Lower bound	Upper bound
τ_0	1	1	1	1
τ_1	0.4	1.2	0.4	0.45
θ_0	0.5	0.5	0.2	0.5
θ_1	0.07	0.10	0.00	0.03

Table 2: Parameters in Eq. (25) used to bound the computed values of K_k in Fig. 11.

by a simple analytical functional form. It is found that

$$K_k = \tau_0 + (\tau_1 + \theta_1 k)(1 - \exp(-k\theta_0/\tau_1)), \tag{25}$$

bounds the calculated K_k from both above and below, as shown in Fig. 11, in both 2D and 3D composites. The parameters corresponding to these bounds are listed in Tab. 2, both for 2D and 3D composites. Let the stress concentrations corresponding to the upper and lower bounds be denoted K_k^{high} and K_k^{low}, respectively. The functional form in Eq. (25) was proposed by Tomé et al. (1984) originally for the purpose of fitting plastic hardening curves. While the curve fits for K_k^{high} and K_k^{low} are tight for the 2D composite, they are not so good for certain k in the 3D composite. For example, the curve fits overestimate the stress concentrations corresponding to $k = 1$, and underestimate the same for $k = 6$. This is because the shape of tight clusters in 3D for certain small k deviates significantly from the ideal of a penny-shaped cluster of breaks.

3.6. The Harlow-Phoenix-Smith cluster growth model

For polymer matrix composites, Harlow and Phoenix (1978a,b) and Smith (1980) proposed a probabilistic model of failure. In their model, composite failure occurs when at least one of n_{f} weakest-link events occurs. That is, there exists a weakest-link strength distribution, independent of n_{f}, and denoted by $W(p)$ such that

$$G_{n_{\mathrm{f}}}(p) = 1 - (1 - W(p))^{n_{\mathrm{f}}}. \tag{26}$$

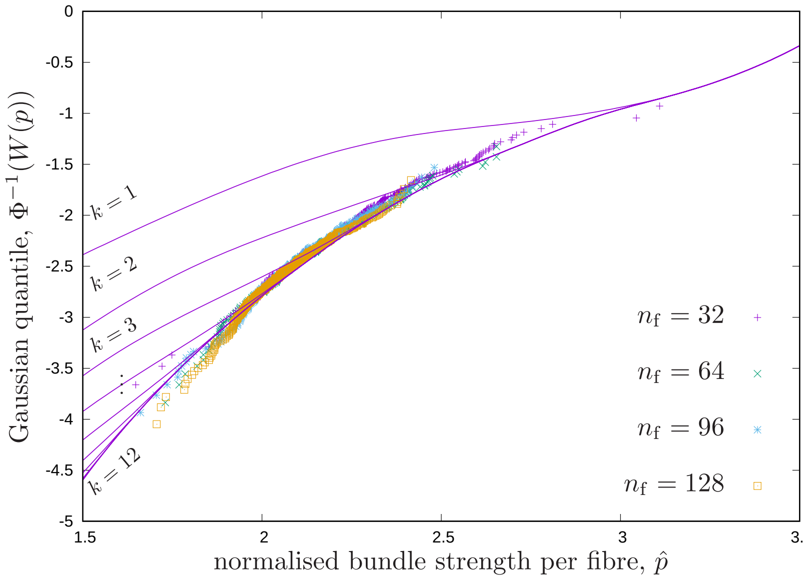

(a) 2D

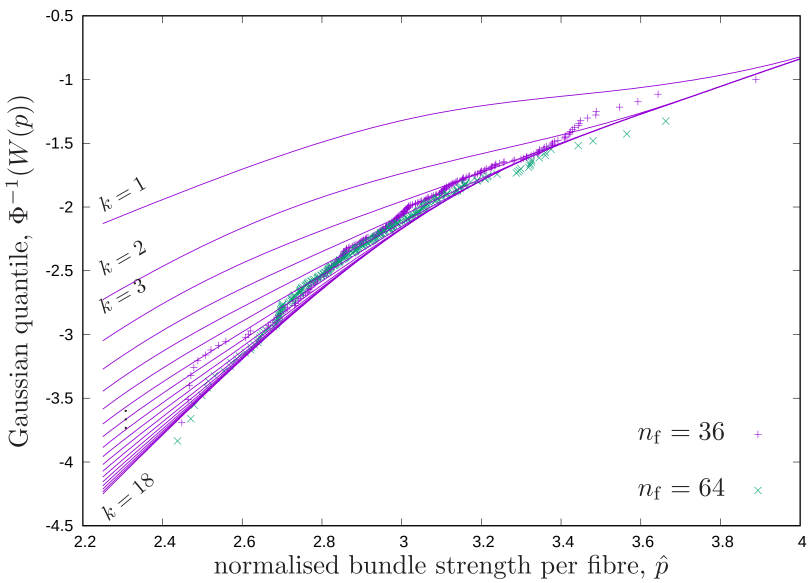

(b) 3D

Figure 12: The empirical weakest-link strength distribution, Eq. (26), is well captured by the Harlow-Phoenix-Smith cluster growth model, Eq. (28), in both (a) 2D and (b) 3D composites.

Fig. 12a shows the weakest-link distribution, $W(p)$, obtained from empirical strength distributions $G_{n_\mathrm{f}}(p)$ for the four sizes $n_\mathrm{f} = 32$, 64, 96 and 128 of 2D composites. The corresponding 3D empirical weakest-link distributions for $n_\mathrm{f} = 36$, and 64 are shown in Fig. 12b. These weakest-link distributions are obtained by inverting Eq. (26). It is seen that the weakest-link distributions obtained from all four sizes in 2D and from the two sizes in 3D collapse onto one master curve, i.e., $W(p)$ is indeed independent of bundle size, n_f. Substituting Eq. (26) into Eq. (16) yields

$$H_{n_\mathrm{f},L}(p) = 1 - (1 - W(p))^{n_\mathrm{f}(L/\Delta L)}. \tag{27}$$

Harlow and Phoenix (1978a,b); Smith (1980) and Smith et al. (1983) also proposed a dominant weakest-link failure event underlying $W(p)$. They proposed that the probability of the weakest-link event equals the probability of development of a tight cluster of breaks. The k-th break in this sequence forms under the stress concentration generated by the $(k-1)$-tight cluster of breaks. These considerations are expressed mathematically as:

$$\begin{aligned} W_k^{\mathrm{model}}(p) = F(E_\mathrm{f}\varepsilon_{\mathrm{engg}};\Delta L) \times \left\{1 - [1 - F(K_1 E_\mathrm{f}\varepsilon_{\mathrm{engg}};\Delta L)]^{N_1}\right\} \times \\ \left\{1 - [1 - F(K_2 E_\mathrm{f}\varepsilon_{\mathrm{engg}};\Delta L)]^{N_2}\right\} \times \ldots \times \left\{1 - [1 - F(K_k E_\mathrm{f}\varepsilon_{\mathrm{engg}};\Delta L)]^{N_k}\right\}, \end{aligned} \tag{28}$$

where, $W_k^{\mathrm{model}}(p)$ is the probability of occurrence of a k-cluster of breaks, K_k denotes the stress concentration due a tight cluster of k breaks, given by Eq. (25), N_k denotes the number of most overloaded intact neighbours of a cluster of k breaks, and $F(\cdot)$ denotes the probability of fibre failure, given by Eq. (18). $\varepsilon_{\mathrm{engg}}$ in the right side of Eq. (28) is obtained by numerically inverting Eq. (15) using successive bisection. The model weakest-link probability is defined as

$$W^{\mathrm{model}}(p) = \lim_{k\to\infty} W_k^{\mathrm{model}}(p). \tag{29}$$

In a 2D composite, the number of most overloaded neighbours of a tight cluster of k fibre breaks, $N_k = 2$ for all $k \geq 1$. In a 3D composite, to a good approximation, it is known that $N_k \approx 2\sqrt{3k} - 1$ (Habeeb and Mahesh, 2015), with the approximation being accurate for $k \geq 2$. Thus,

$$N_k = \begin{cases} 2, & \text{in a 2D model composite, and} \\ 2\sqrt{3k} - 1, & \text{in a 3D model composite.} \end{cases} \tag{30}$$

Employing the upper and lower bound parameters for K_k from Tab. 2 leads to overprediction and under-prediction of the weakest-link strength distribution (not shown). Thus neither $K_k^{\rm high}$ nor $K_k^{\rm low}$ is a tight bound on the stress concentration, K_k. A simple interpolative formula given by

$$K_k = \exp(-k/k_0) K_k^{\rm low} + (1 - \exp(-k/k_0))\, K_k^{\rm high}, \tag{31}$$

with $k_0 = 4$, however, leads to the predictions of $W_k^{\rm model}(p)$, $k = 1, 2, \ldots, 12$, shown in Fig. 12a for 2D composites, and with $k_0 = 2$ to the predictions of $W_k^{\rm model}(p)$, $k = 1, 2, \ldots, 18$, for 3D composites, as shown in Fig. 12b. In both cases, it is clearly seen that the lower envelope of the predicted $W_k^{\rm model}(p)$ agrees well with the empirical weakest-link distribution. Eq. (31) merely represents a plausible smooth transition from $K_k^{\rm low}$ to $K_k^{\rm high}$ with increasing k. Its form is not based on physical considerations.

Figs. 12a and 12b show that convergence of $W_k^{\rm model}(p)$ in the sense of Eq. (29) occurs for smaller k at larger bundle strengths, p. The lower tail of the weakest-link distribution thus corresponds to larger k, exactly as in the reliability theory of polymer matrix composites.

3.7. Size scaling of strength for prescribed reliability levels

Some components in an engine are more critical than others. For example, the engine risk due to the failure of bladed disks, bladed rings, and impellers is rated high, that due to fan and compressor blades is rated moderate, and that due to spacers is rated low (Singerman and Jackson, 1996, Table II). The acceptable failure probability, q, of bladed disks, bladed rings, and impellers must be lowest (say, $q = 10^{-6}$), that of fan and compressor blades intermediate (say, $q = 10^{-4}$), while that of spacers can be relatively higher (say, $q = 10^{-2}$).

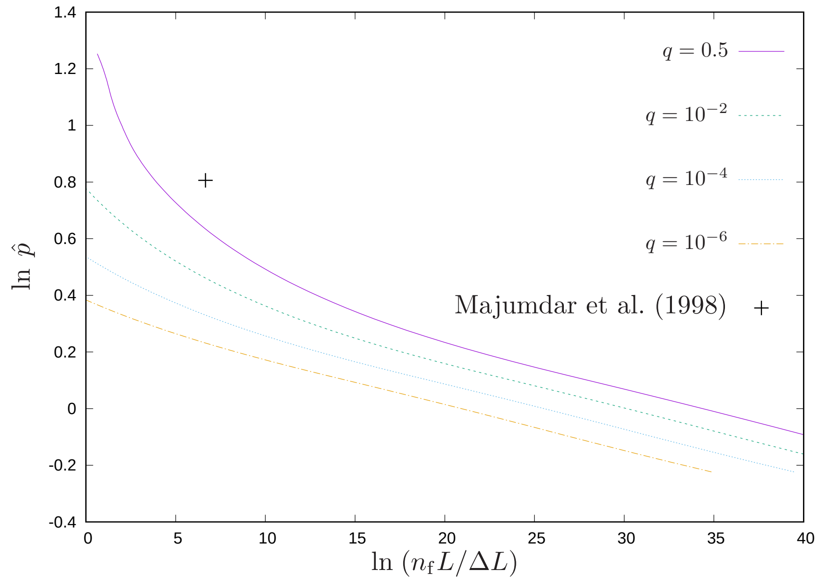

(a) 2D

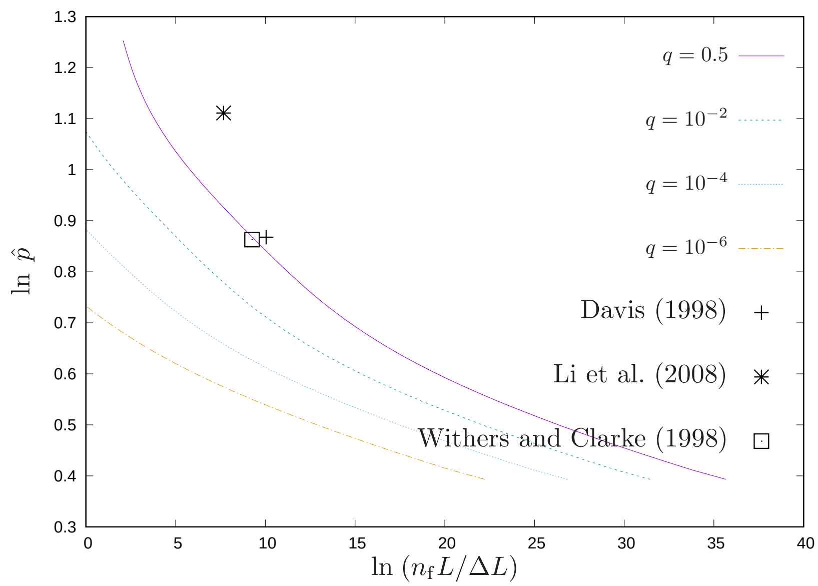

(b) 3D

Figure 13: Size-scaling of bundle strength for four failure probability levels, q in (a) 2D, and (b) 3D composites. The predicted mean strength corresponds to $q = 0.5$. Reliable material strength decreases with increasing reliability and composite size. Experimental data points obtained from the literature are discussed in the text below.

The relationship between the composite size, $n_{\mathrm{f}}L/\Delta L$, and composite strength, $\hat{p}$ is now deduced for an arbitrarily specified acceptable failure probability, $0 < q < 1$. That is, given a bundle failure probability, $q \in (0, 1)$, the relationship between $n_{\mathrm{f}}L/\Delta L$, and $\hat{p}$ is determined by requiring that

$$H_{n_{\mathrm{f}},L}(p) = q. \tag{32}$$

It follows from substituting Eq. (27) into Eq. (32) that

$$n_{\mathrm{f}}L/\Delta L = \ln(1-q)/\ln(1-W(p))). \tag{33}$$

Using the approximation $W(p) \approx W^{\mathrm{model}}(p)$ (Eq. (29)) in Eq. (33) gives the size-scaling with strength for various acceptable failure probabilities, q. Scaling curves corresponding to the mean strength $q = 0.5$, and to higher reliability levels, $q = 10^{-2}$, 10^{-4} and 10^{-6}) are plotted in Figs. 13a and 13b for the 2D and 3D model composites, respectively.

3.8. Comparison with experiments

The present results are now compared with experimental data from the literature on 2D and 3D composites. In each case, the fibre (SCS-6 SiC) and matrix (Ti-6Al-4V) materials of the present study are nominally the same as those in the experimental material. However, details of material processing and the spatial distribution of fibres may different.

Majumdar et al. (1998) report a tensile strength of 1160 MPa for a 2D $n_{\mathrm{f}} = 40$-fibre composite of guage length 25.4 mm. In order to prevent composite fracture in the shoulders of their test coupon, Majumdar et al. (1998) employed a thick matrix cladding, resulting in a fibre volume fraction of only 11.6%. To compare with the present model, their specimen is idealised as two matrix strips of thickness 270 μm sandwiching a fibre-reinforced strip of ply thickness $d = 124$ μm. If the 270 μm thick cladding were taken to carry a uniform flow stress of 900 MPa at the point of composite failure, as suggested by Majumdar et al. (1998, Fig. 4), the effective stress in the fibre-reinforced central region comes out to be 2274 MPa. This amounts to force per fibre of 56.9 N, which when non-dimensionalised following Eq. (22) yields $\hat{p} = 2.24$. Further, for this specimen, $n_\mathrm{f}L/\Delta L = 40 \times 25.4/1.3 \approx 781$. The $(n_\mathrm{f}L/\Delta L, \hat{p})$ point is shown in Fig. 13a. The measured point falls above the $q = 0.5$ curve, i.e., Majumdar et al.'s experimental specimen is found to be stronger than the average model specimen at this size.

For 3D composites, the ASM metals handbook (Davis, 1998) lists the average strength of SiC fibre reinforced Ti-6Al-4V composite with 37% fibre volume fraction as 1447 MPa. Assuming that the fibres are arranged in a hexagonal lattice, the fibre volume fraction corresponds to a centre-to-centre fibre spacing of about 220 μm, which is only slightly smaller than the present assumption of $b = 240$ μm in Table 1. The ultimate tensile force per fibre then works out to $p = 60.5$ N, or in non-dimensional terms, using Eq. (22), $\hat{p} = 2.39$. The cross-sectional area of an ASTM D3552 straight sided standard tensile sample (ASTM, 2017), 10 plies thick is 10.00×1.43 mm^2, and its gage length is $L = 88.0$ mm. For 37% volume fraction, this corresponds to $n_\mathrm{f}L/\Delta L = 2.3 \times 10^4$. The $(n_\mathrm{f}L/\Delta L, \hat{p})$ point corresponding to the test data is shown in Fig. 13b. It is seen that the average test data ($\hat{p} = 2.39$) is only slightly greater than the predicted $q = 0.5$ value ($\hat{p} = 2.32$), an error of about 3%. This shows that the present predictions based on the 'chain of bundles' model described in Sec. 2.5 are not too conservative.

Points corresponding to the single tensile tests reported by Withers and Clarke (1998), and the average of the three tests of Li et al. (2008) are also shown in Fig. 13b. It is seen that the former data point nearly falls on the predicted average strength, but the latter is considerably stronger.

It is important to note that the fabrication route affects the extent of damage imparted to the fibres, and thereby, the average tensile strength. The aforementioned strength of 1447 MPa corresponds to a fabrication route wherein multiple 2D plies are consolidated by hot pressing to form a 3D composite. A much higher average strength (1820 MPa at only 33% fibre volume fraction) is reportedly obtained by triode sputtering, which introduces minimal damage to the fibres (Vassel, 1999). The present model may predict these higher strengths, provided the Weibull strength parameters of the fibres are modified to reflect their more pristine surface condition in the triode sputtered material.

Because the diameter of SiC fibres is significantly greater than that of carbon or glass fibres used to reinforce polymer matrix composites, usually, only modest extrapolation is needed to predict the strength of components for a certain q. For example, consider the metal matrix composite core of the bladed ring described by Moriya et al. (1999). Their fibre and matrix materials are nominally the same as those in the present study. It is therefore reasonable to assume $\Delta L = \delta_c = 1.3$ mm. The reinforcing composite ring has a mean circumference of about 500 mm and is comprised of about 10^4 fibres in a cross-section. The number of weakest-link sites is therefore $n_\mathrm{f} = 10^4 \cdot 500/1.3 \approx 4 \times 10^6$, which is only two orders of magnitude greater than that of an ASTM standard specimen.

3.9. Curtin's weakest-link scaling

An alternate approach to understanding the strength distribution has been proposed by Ibnabdeljalil and Curtin (1997) for ceramic or metal matrix composites with weak interfaces, and by Curtin (1998b) for polymer matrix composites. From Monte Carlo simulations, these authors observed that there exists a critical sub-bundle size m_f such that the bundle fails when any of the critically sized sub-bundles fail, so that

$$G_{n_\mathrm{f}}(p) = 1 - (1 - W_{m_\mathrm{f}}(p))^{n_\mathrm{f}/m_\mathrm{f}}\,. \tag{34}$$

Going further, Curtin (1998b) found that $W_{m_\mathrm{f}}(p)$ has the same normal strength distribution as a Daniels bundle of m_f fibres, with the same standard deviation, but possibly a different mean strength. The scaling given by Eq. (34) was applied to a Ti metal matrix composite by Xia et al. (2001).

Fig. 14a plots the weakest-link strength distribution, as given by Eq. (34), deduced from $G_{n_\mathrm{f}}(p)$ corresponding to the four 2D bundle sizes $n_\mathrm{f} = 32$, 64, 96 and 128. In all cases, the sub-bundle size was taken as $m_\mathrm{f} = 30$. Fig. 14a shows that the weakest-link strength distribution, $W_{m_\mathrm{f}=30}(p)$, plots on Gaussian paper as a straight line in the upper and middle parts of the distribution.

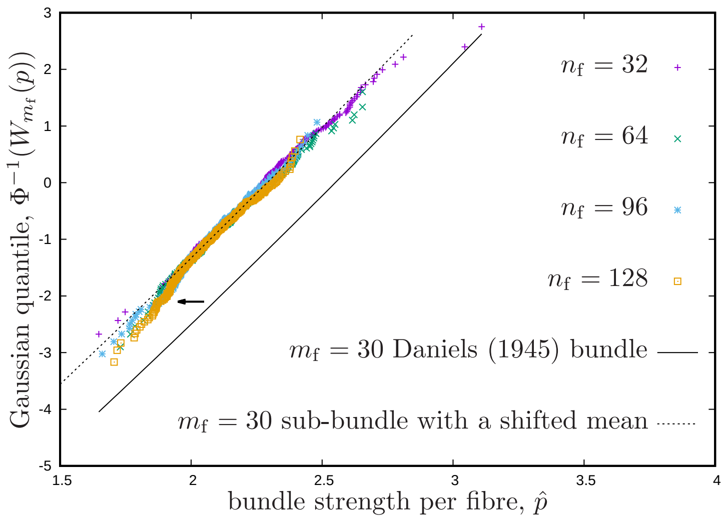

(a) 2D

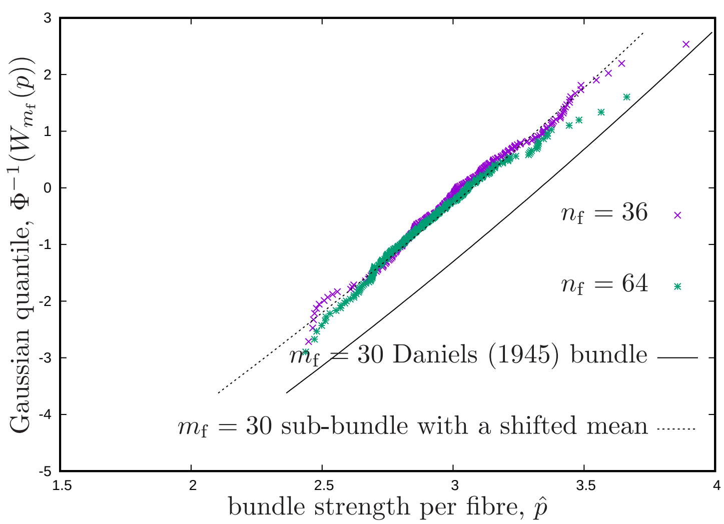

(b) 3D

Figure 14: Empirical strength distributions of (a) 2D composite bundles comprised of $n_\mathrm{f} = 32$, 64, 96, and 128 fibres, and (b) 3D composite bundles comprised of $n_\mathrm{f} = 36$, and 64 fibres. Both 2D and 3D distributions are weak-linked to a critical size of $m_\mathrm{f} = 30$. In both (a) and (b), the solid line is the Daniels (1945) strength distribution predicted for a loose bundle of $m_\mathrm{f} = 30$ fibres. The dashed line is the solid line shifted horizontally through -0.26 in both (a) and (b).

Over this part, $W_{m_\mathrm{f}=30}(p)$ agrees well in slope (reciprocal standard deviation) with the strength distribution predicted by Daniels (1945) for an equal load sharing bundle of 30 fibres. Such coincidence does not occur for other values of m_f. However, the mean strengths of the present bundle and the Daniels bundle do not agree; an imposed shift in the mean strength is necessary to bring the empirical $W_{m_\mathrm{f}=30}(p)$ into coincidence with the Daniels bundle strength. In the lower tail, however, the downward curvature of the empirical weakest-link strength distributions indicates deviation from normality in the lower tail. The beginning of the lower tail is indicated by the arrow in Fig. 14. This observation suggests that Eq. (34) should not be employed to extrapolate the strength distributions into the lower tail.

Fig. 14b depicts the weakest-link strength distribution for 3D composites with bundle sizes of $n_\mathrm{f} = 36$, and 64 fibres. This figure also shows the strength distribution predicted for a Daniels bundle with $m_\mathrm{f} = 30$. Surprisingly, the best agreement of the weakest-link strength distribution with Daniels bundle strength occurs by taking the same m_f and imposed shift in the mean strength as in 2D. This is noteworthy, because the Gaussian bundle strength is independent of the dimensionality of the composite. In the lower tail, $W_{m_\mathrm{f}=30}(p)$ deviates from the distribution of Daniels' bundle strength. This deviation is less pronounced than in 2D. This is reasonable because the stress concentrations, and hence tendency toward local load sharing in 3D composites is lower than that in 2D composites.

It may be noticed that the strength of a Daniels bundle comprised of $m_\mathrm{f} = 30$ fibres plots as two distinct lines in 2D and 3D in Fig. 14. This is because for a given $\hat{p}$, the far-field strain ε_f obtained from Eq. (15) are distinct in 2D and 3D, as the number of tensile matrix elements in the latter is thrice as many as in the former (Eq. (2)).

The upper and middle tail of the empirical weakest-link strength distribution can be explained by two different stochastic models: the Harlow-Phoenix-Smith cluster growth model (Eq. (28)), and Curtin's global failure model (Eq. (34)). The two models however, diverge from each other in the lower tail. Fig. 15 shows the extrapolated predictions of both models into the deep lower tail, in

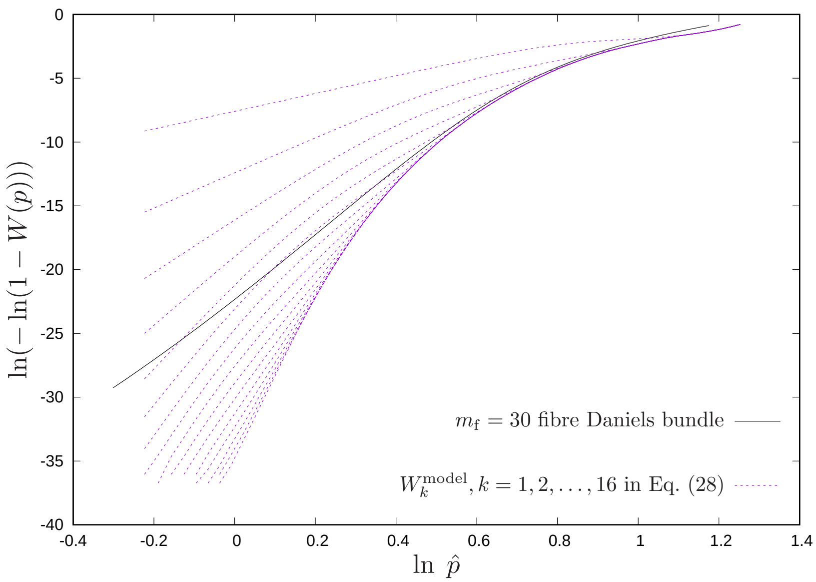

(a) 2D

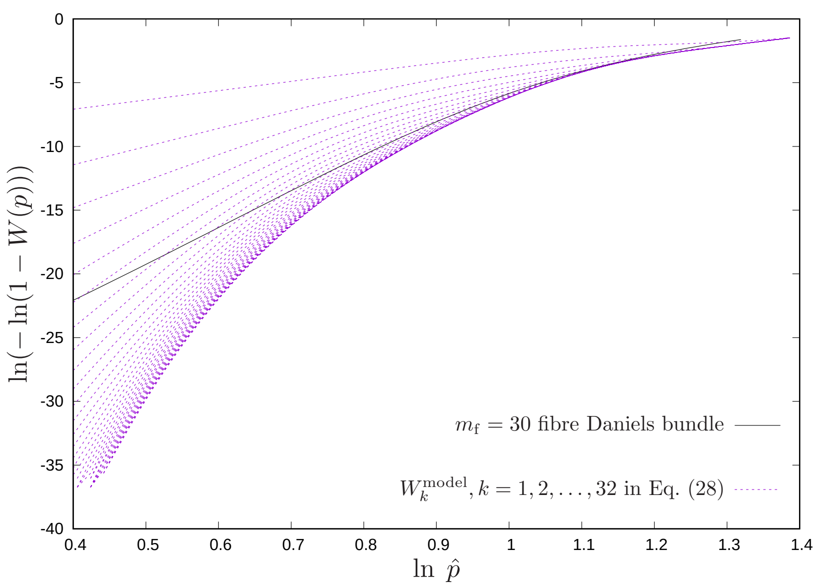

(b) 3D

Figure 15: Comparison of the extrapolated predictions of the Harlow-Phoenix-Smith cluster growth model (Eq. (28)), and Curtin's global failure model (Eq. (34)) in the deep lower tail, for (a) 2D and (b) 3D composites.

Weibull probability coordinates. The comparison shows that the Curtin global failure model is conservative in the regime of the lower tail in both 2D and 3D composites.

4. Conclusions

Using a recently developed shear-lag model (Mishra and Mahesh, 2017), 2D and 3D Monte Carlo failure simulations of sizeable Ti/SiC fibre composites have been performed while accounting for non-linear effects associated with the matrix and interfacial response and their interactions. The simulations overcome the limitations of earlier studies, which were either restricted to composites comprised of very few fibres (Liu and Zheng, 2006) or used approximate estimates of the stress state based on the linear superposition principle Xia et al. (2001). The present model itself, however, suffers from the limitation of not resolving the three-dimensional stress state, on account of its shear-lag character. The composite is also modeled as a chain of bundles in the present work, so that the three-dimensional interactions between fibre breaks are treated somewhat simplistically, but conservatively.

Using Monte Carlo simulations, and probabilistic modelling, it has been shown that the strength of a single ply commercial Ti/SiC composite obeys the classical Harlow-Phoenix-Smith weakest-link strength distribution (Harlow and Phoenix, 1978a,b; Smith, 1980), originally developed for local load sharing polymer matrix composites. A strongly clustered mode of breaking is observed from the simulations. This is consistent with experimental observations reported in the literature (Gundel and Wawner, 1997; González and Llorca, 2001; Li et al., 2008). Specimen strengths predicted by the model are also in reasonable agreement with those reported in the literature. The stochastic model, validated against empirical distributions generated by Monte Carlo simulations, can be used to extrapolate the metal matrix strength distribution into the lower tail. Most usefully, this model predicts the safe working loads for any desired level of reliability, which in turn depends on component criticality (Singerman and Jackson, 1996).

The empirical distributions obtained from the present simulations are also compared with the stochastic model proposed by Xia et al. (2001). For a suitably selected link-length, it was found that the stochastic model of Xia et al. (2001) could capture the upper and middle tails of the present empirical distributions well. In the lower tail, however, the weakest-link distribution proposed by Xia et al. (2001) overestimates the failure probabilities, i.e., is too conservative. This effect is more pronounced in 2D on account of greater stress concentrations ahead of a fixed number of breaks, than in 3D composites.

E. Martin, N. Carrére, Metal Matrix Composites: Continuous Silicon-Carbide Fibers/Titanium-Alloy Matrix, Wiley Encyclopedia of Composites .

S. Singerman, J. Jackson, Titanium metal matrix composites for aerospace applications, in: Superalloys 1996, 579–586, 1996.

S. Mahesh, S. Phoenix, I. Beyerlein, Strength distributions and size effects for 2D and 3D composites with Weibull fibers in an elastic matrix, Int J Fracture 115 (1) (2002) 41–85.

W. Curtin, Stochastic damage evolution and failure in fiber-reinforced composites, Advances in applied mechanics 36 (1998a) 163–253.

S. L. Phoenix, I. Beyerlein, Statistical strength theory for fibrous composite materials, Comprehensive composite materials 1 (2000) 559–639.

T. Okabe, N. Takeda, Y. Kamoshida, M. Shimizu, W. Curtin, A 3D shear-lag model considering micro-damage and statistical strength prediction of unidirectional fiber-reinforced composites, Compos. Sci. Tech. 61 (12) (2001) 1773–1787.

I. Beyerlein, C. Landis, Shear-lag model for failure simulations of unidirectional fiber composites including matrix stiffness, Mech. Mater. 31 (5) (1999) 331–350.

S. Pimenta, S. Pinho, Hierarchical scaling law for the strength of composite fibre bundles, J Mech Phys Solids 61 (6) (2013) 1337–1356.

S. Behzadi, P. Curtis, F. Jones, Improving the prediction of tensile failure in unidirectional fibre composites by introducing matrix shear yielding, Compos Sci Tech 69 (14) (2009) 2421–2427.

W. Curtin, Theory of Mechanical Properties of Ceramic-Matrix Composites, J Am Ceramic Soc 74 (11) (1991) 2837–2845.

S. Phoenix, R. Raj, Scalings in fracture probabilities for a brittle matrix fiber composite, Acta metall mater 40 (11) (1992) 2813–2828.

W. Curtin, Ultimate strengths of fibre-reinforced ceramics and metals, Composites 24 (2) (1993) 98–102.

Z. Xia, W. Curtin, P. Peters, Multiscale modeling of failure in metal matrix composites, Acta Mater. 49 (2) (2001) 273–287.

A. Mishra, S. Mahesh, A deformation-theory based model of a damaged metal matrix composite, Int. J. Solids Struct. 121 (2017) 228–239.

D. Gundel, F. Wawner, Experimental and theoretical assessment of the longitudinal tensile strength of unidirectional SiC-fiber/titanium-matrix composites, Compos sci tech 57 (4) (1997) 471–481.

C. González, J. Llorca, Micromechanical modelling of deformation and failure in Ti–6Al–4V/SiC composites, Acta Mater. 49 (17) (2001) 3505–3519.

U. Ramamurty, Assessment of load transfer characteristics of a fiber-reinforced titanium-matrix composite, Composites science and technology 65 (11-12) (2005) 1815–1825.

J.-K. Li, Y.-Q. Yang, M.-N. Yuan, L. Xian, L.-L. Li, Effect of properties of SiC fibers on longitudinal tensile behavior of SiCf/Ti-6Al-4V composites, Transactions of Nonferrous Metals Society of China 18 (3) (2008) 523–530.

D. Harlow, S. Phoenix, The chain-of-bundles probability model for the strength of fibrous materials I, J. compos. mater. 12 (2) (1978a) 195–214.

D. Harlow, S. Phoenix, The chain-of-bundles probability model for the strength of fibrous materials II, J. compos. mater. 12 (3) (1978b) 314–334.

R. Smith, A probability model for fibrous composites with local load sharing, Proc R Soc Lond A 372 (1751) (1980) 539–553.

M. Winstone, A. Partridge, J. Brooks, The contribution of advanced high-temperature materials to future aero-engines, Proc. Inst. Mech. Eng. L J. Mater. Des. Appl. 215 (2) (2001) 63–73.

J. Hanan, E. Üstündag, I. Beyerlein, G. Swift, J. Almer, U. Lienert, D. Haeffner, Microscale damage evolution and stress redistribution in Ti–SiC fiber composites, Acta materialia 51 (14) (2003) 4239–4250.

B. Majumdar, T. Matikas, D. Miracle, Experiments and analysis of fiber fragmentation in single and multiple-fiber SiC/Ti-6Al-4V metal matrix composites, Composites Part B: Engineering 29 (2) (1998) 131–145.

C. M. Landis, R. M. McMeeking, A shear-lag model for a broken fiber embedded in a composite with a ductile matrix, Compos. Sci. Tech. 59 (3) (1999) 447–457.

P. Withers, A. Clarke, A neutron diffraction study of load partitioning in continuous Ti/SiC composites, Acta mater 46 (18) (1998) 6585–6598.

D. Gücer, J. Gurland, Comparison of the statistics of two fracture modes, J Mech Phys Solids 10 (4) (1962) 365–373.

J. Liu, P. Bowen, Strength of SCS-6 fibers in a Tiβ21s/SCS-6 composite before and after fatigue, Metal Mater Trans A 34 (5) (2003) 1203–1213.

M. Abramowitz, I. Stegun, Handbook of Mathematical Functions: with Formulas, Graphs, and Mathematical Tables, Dover Publications, 2012.

R. Henstenburg, S. Phoenix, Interfacial shear strength studies using the single-filament-composite test: Part II, Polymer compos 10 (6) (1989) 389–408.

W. Curtin, Dimensionality and size effects on the strength of fiber-reinforced composites, Composites Science and Technology 60 (4) (2000) 543–551.

I. Beyerlein, S. Phoenix, Stress concentrations around multiple fiber breaks in an elastic matrix with local yielding or debonding using quadratic influence superposition, J. Mech. Phys. Solids 44 (12) (1996) 1997–2039.

S. Mahesh, S. Phoenix, Lifetime distributions for unidirectional fibrous composites under creep-rupture loading, Int J Fract 127 (4) (2004) 303–360.

H. Daniels, The statistical theory of the strength of bundles of threads. I, Proc. R. Soc. Lond A 183 (995) (1945) 405–435.

L. McCartney, R. Smith, Statistical theory of the strength of fiber bundles, Journal of applied mechanics 50 (3) (1983) 601–608.

T. Pini, F. Caimmi, F. Briatico-Vangosa, R. Frassine, M. Rink, Fracture initiation and propagation in unidirectional CF composites based on thermoplastic acrylic resins, Engineering Fracture Mechanics 184 (2017) 51–58.

R. Smith, S. Phoenix, M. Greenfield, R. Henstenburg, R. Pitt, Lower-tail approximations for the probability of failure of three-dimensional fibrous composites with hexagonal geometry, Proc. R. Soc. Lond. A 388 (1795) (1983) 353–391.

C. Tomé, G. Canova, U. Kocks, N. Christodoulou, J. Jonas, The relation between macroscopic and microscopic strain hardening in FCC polycrystals, Acta metall 32 (10) (1984) 1637–1653.

C. Habeeb, S. Mahesh, Strength distribution of planar local load-sharing bundles, Physical Review E 92 (2) (2015) 022125.

C. Sun, J. Chen, G. Sha, W. Koop, Mechanical characterization of SCS-6/Ti-6-4 metal matrix composite, J. Composite Mater 24 (10) (1990) 1029–1059.

J. R. Davis (Ed.), Metals handbook, Desk edition, chap. Metal matrix composites, ASM International, 2 edn., 1626, 1998.

ASTM, Standard Test Methods for Tension Testing of Fiber Reinforced Metal Matrix Composites, Standard D 3552, ASTM, West Conshohocken PA, 2017.

A. Vassel, Continuous fibre reinforced titanium and aluminium composites: a comparison, Materials Science and Engineering: A 263 (2) (1999) 305–313.

K. Moriya, Y. Nojima, S. Nishide, K. Yasuhira, Fabrication of titanium metal matrix composite bling, in: Proceedings of ICCM-12, no. 415 in 12, International committee on composite materials, Paris, 415, 1999.

M. Ibnabdeljalil, W. Curtin, Strength and reliability of fiber-reinforced composites: localized load-sharing and associated size effects, Int J Solids Struct 34 (21) (1997) 2649–2668.

W. Curtin, Size scaling of strength in heterogeneous materials, Phys Rev Lett 80 (7) (1998b) 1445.

P. Liu, J. Zheng, A Monte Carlo finite element simulation of damage and failure in SiC/Ti–Al composites, Mater Sci. Eng. A 425 (1) (2006) 260–267.